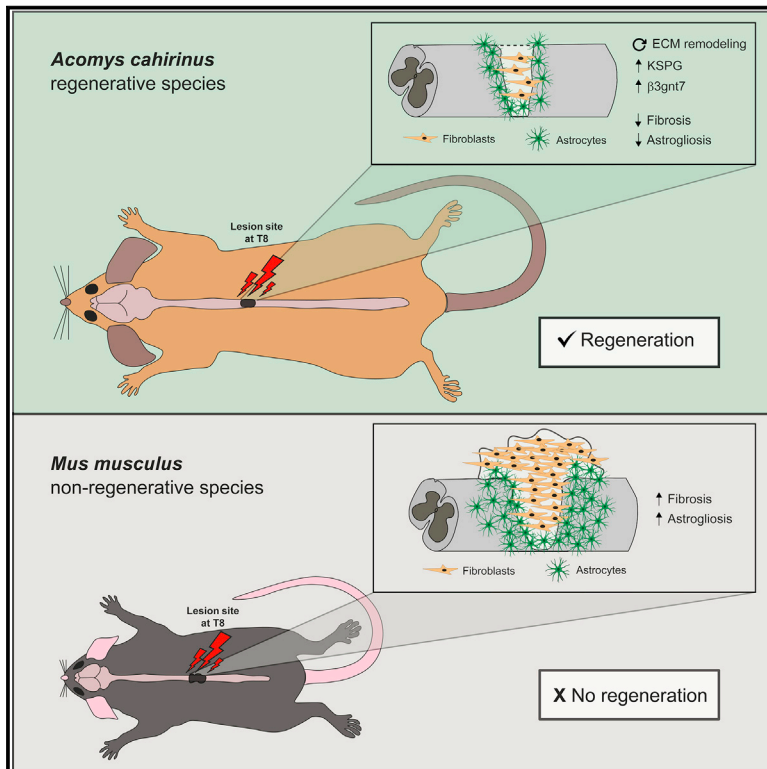


Developmental Cell

Rewired glycosylation activity promotes scarless regeneration and functional recovery in spiny mice after complete spinal cord transection

Graphical abstract



Authors

Joana Nogueira-Rodrigues,
Sérgio C. Leite, Rita Pinto-Costa, ...,
Gustavo Tiscórnia, Inês M. Araújo,
Mónica M. Sousa

Correspondence

msousa@ibmc.up.pt

In brief

Nogueira-Rodrigues et al. report that *Acomys* can recover function after complete spinal cord injury (SCI), assembling a scarless tissue at the injury site, unlike other adult mammals. Transcriptomic analysis of the SCI site shows that injured *Acomys* builds a specific pro-regenerative proteoglycan signature with a unique glycosylation network.

Highlights

- *Acomys* spontaneously regains motor and urinary functions following complete SCI
- The *Acomys* SCI site shows abundant axon regeneration and nerve conduction
- *Acomys* assembles a pro-regenerative environment with rewired ECM glycosylation
- $\beta 3gnt7$ is a novel axon regeneration enhancer



Short Article

Rewired glycosylation activity promotes scarless regeneration and functional recovery in spiny mice after complete spinal cord transection

Joana Nogueira-Rodrigues,^{1,2} Sérgio C. Leite,¹ Rita Pinto-Costa,¹ Sara C. Sousa,^{1,2} Liliana L. Luz,³ Maria A. Sintra,¹ Raquel Oliveira,^{4,5,6} Ana C. Monteiro,¹ Gonçalo G. Pinheiro,^{7,8} Marta Vitorino,^{7,8} Joana A. Silva,⁸ Sónia Simão,^{8,9} Vitor E. Fernandes,^{8,9} Jan Provazník,¹⁰ Vladimír Benes,¹⁰ Célia D. Cruz,^{4,5} Boris V. Safronov,³ Ana Magalhães,^{11,12} Celso A. Reis,^{11,12,13} Jorge Vieira,¹⁴ Cristina P. Vieira,¹⁴ Gustavo Tiscornia,^{7,15,17} Inês M. Araújo,^{8,9,16,17} and Mónica M. Sousa^{1,17,18,*}

¹Nerve Regeneration Group, Instituto de Biologia Molecular e Celular (IBMC), Instituto de Investigação e Inovação em Saúde (i3S), University of Porto, 4200-135 Porto, Portugal

²Graduate Program in Molecular and Cell Biology, Instituto de Ciências Biomédicas Abel Salazar (ICBAS), University of Porto, 4050-313 Porto, Portugal

³Neuronal Networks Group, Instituto de Biologia Molecular e Celular (IBMC), Instituto de Investigação e Inovação em Saúde (i3S), University of Porto, 4200-135 Porto, Portugal

⁴Translational NeuroUrology Group, Instituto de Biologia Molecular e Celular (IBMC), Instituto de Investigação e Inovação em Saúde (i3S), University of Porto, 4200-135 Porto, Portugal

⁵Department of Biomedicine, Experimental Biology Unit, Faculty of Medicine of Porto, University of Porto, 4200-319 Porto, Portugal

⁶Regeneration Group, Wolfson Centre for Age-Related Diseases, Institute of Psychiatry, Psychology and Neuroscience, King's College London WC2R 2LS, London, UK

⁷Molecular & Regenerative Medicine Laboratory, Centro de Ciências do Mar (CCMAR), University of Algarve, 8005-139 Faro, Portugal

⁸Faculty of Medicine and Biomedical Sciences, University of Algarve, 8005-139 Faro, Portugal

⁹Algarve Biomedical Center Research Institute (ABC-RI), University of Algarve, 8005-139 Faro, Portugal

¹⁰Genomics Core Facility, European Molecular Biology Laboratory (EMBL), 69117 Heidelberg, Germany

¹¹Glycobiology in Cancer Group, Institute of Molecular Pathology and Immunology, IPATIMUP, Instituto de Investigação e Inovação em Saúde (i3S), University of Porto, 4200-135 Porto, Portugal

¹²Department of Molecular Biology, Instituto de Ciências Biomédicas Abel Salazar (ICBAS), University of Porto, 4050-313 Porto, Portugal

¹³Department of Pathology, Faculty of Medicine of Porto, University of Porto, 4200-319 Porto, Portugal

¹⁴Phenotypic Evolution Group, Instituto de Biologia Molecular e Celular (IBMC), Instituto de Investigação e Inovação em Saúde (i3S), University of Porto, 4200-135 Porto, Portugal

¹⁵Clinica Eugén, Research and Development, 08006 Barcelona, Spain

¹⁶Champalimaud Research Program, Champalimaud Center for the Unknown, 1400-038 Lisbon, Portugal

¹⁷These authors contributed equally

¹⁸Lead contact

*Correspondence: msousa@ibmc.up.pt

<https://doi.org/10.1016/j.devcel.2021.12.008>

SUMMARY

Regeneration of adult mammalian central nervous system (CNS) axons is abortive, resulting in inability to recover function after CNS lesion, including spinal cord injury (SCI). Here, we show that the spiny mouse (*Acomys*) is an exception to other mammals, being capable of spontaneous and fast restoration of function after severe SCI, re-establishing hind limb coordination. Remarkably, *Acomys* assembles a scarless pro-regenerative tissue at the injury site, providing a unique structural continuity of the initial spinal cord geometry. The *Acomys* SCI site shows robust axon regeneration of multiple tracts, synapse formation, and electrophysiological signal propagation. Transcriptomic analysis of the spinal cord following transcriptome reconstruction revealed that *Acomys* rewires glycosylation biosynthetic pathways, culminating in a specific pro-regenerative proteoglycan signature at SCI site. Our work uncovers that a glycosylation switch is critical for axon regeneration after SCI and identifies $\beta 3gnt7$, a crucial enzyme of keratan sulfate biosynthesis, as an enhancer of axon growth.

INTRODUCTION

After trauma, mature mammalian central nervous system (CNS) axons largely fail to regenerate. This inability of adult mammals to regrow their axons is a major obstacle in the treatment of

CNS injuries, including spinal cord injury (SCI) that remains an unmet medical condition. Despite the efforts and considerable progress over the past decades in the scientific knowledge, and in the medical, surgical, and rehabilitative care of SCI patients, there are currently no effective treatments to improve their



neurologic outcome. The unsuccessful regeneration of CNS axons is largely caused by scarring at the injury site (Cregg et al., 2014), that creates a physical barrier and inhibitory chemical environment for axon regrowth. After CNS injury, fibroblasts proliferate into the lesion core and repress axon elongation through the expression of repulsive axon guidance molecules and inhibitory extracellular matrix (ECM) components (Dias and Goritz, 2018; Giger et al., 2010), dictating tissue fibrosis. Astrocytes, also recruited to the injury site, undergo phenotypic changes and become reactive scar-forming cells, further secreting inhibitory molecules (Okada et al., 2018; Yang et al., 2020).

Outside the CNS, mammalian tissue regeneration is also a rare event. The spiny mouse (*Acomys cahirinus*), a member of the *Muridae* family (together with *Mus musculus* and *Rattus norvegicus*, widely used in biomedical research), emerged as a curious exception as it sustains scar-free regeneration of the skin (Seifert et al., 2012) and ear (Gawriluk et al., 2016; Matias Santos et al., 2016). Recently, following a minor lateral, dorsal crush injury of the spinal cord, *Acomys* was shown to have reduced spinal inflammation and fibrosis, suggesting that this species might be a useful model to study SCI (Streeter et al., 2020). A growing body of evidence demonstrates that, in contrast with most other mammals that heal their wounds by fibrotic scarring, *Acomys* exhibits decreased fibrosis after wounding (Brant et al., 2015, 2016; Seifert et al., 2012), and an altered inflammatory response (Cyr et al., 2019; Gawriluk et al., 2020; Simkin et al., 2017).

Given the unprecedented capacity of the injured *Acomys* skin and ear to heal after wounding, we explored the possibility that the *Acomys* CNS might also regenerate. Here, we reveal that *Acomys* is able to do what no other adult mammal can: spontaneously regenerate its spinal cord after complete transection with fast restoration of function. Our data show that *Acomys* assembles a pro-regenerative environment at the injury site with rewired glycosyltransferase activity, dictating a specific proteoglycan signature. Our results disclose the spiny mouse as a valuable model to explore the molecular mechanisms enabling robust functional axon regeneration in the adult mammalian CNS.

RESULTS

Acomys spontaneously recovers function following complete spinal cord transection

To test if the spiny mouse regenerative capacity extends to the CNS, complete spinal cord transection was performed at T8 in *Acomys cahirinus* (Figure 1A) and in the non-regenerative control *Mus musculus*. All sham and injured animals were tested during 8 weeks post-injury (WPI) to assess functional recovery (Figure 1B). Remarkably, *Acomys* started to regain motor function at 2 WPI showing an average Basso mouse scale (BMS) score of 2 (i.e., extensive ankle movement), whereas *Mus* remained with the initial BMS score of 0 (i.e., no ankle movement) (Figures 1C and 1D). At the final time point (8 WPI), *Acomys* presented an average final BMS score of 4, which implies the re-establishment of the initial weight support with occasional plantar stepping (Figure 1D). Of note, at 8 WPI, 8 out of 14 injured *Acomys* gained full weight support being able to stand on their hind limbs and presented consistent plantar stepping and a restored pattern of fore and hind limb coordination (Figures 1C and 1D; Video S1).

In contrast, injured *Mus* had a dysfunctional locomotor pattern in which plantar stepping and weight support were severely compromised (Figures 1C and 1D; Video S2). *Acomys* were re-injured at 8 WPI to further verify that motor recovery is caused by axon regeneration. The second complete lesion generated the immediate decrease of the BMS score to 0 (Figure 1D). Of note, at 8 WPI, other *Mus* strains do not show BMS scores comparable to the ones here described for *Acomys*. Even in the case of MRL/MpJ mice, a *Mus* strain with enhanced axon regeneration, when gait of lesioned animals is evaluated, no statistical differences were found when compared with injured C57BL/6 mice (Thuret et al., 2012).

SCI usually abolishes voluntary control of micturition and SCI-related bladder dysfunction is a major concern for patients as it poses a significant risk to their well-being (Hamid et al., 2018). Exceptionally, injured *Acomys* regained normal bladder control at 3 WPI, whereas *Mus* required manual bladder voidance throughout the entire recovery period (Figure 1E). Upon SCI, *Mus* presented common features of bladder dysfunction including urine leakage in random and small spots (Figures 1F and 1G) and a decreased volume of voided urine compared with sham-operated animals (Figure 1H), suggesting urine retention in the bladder. While *Mus* presented a micturition disability with periods of incontinence, from 1 WPI on, injured *Acomys* were indistinguishable from sham *Acomys* (Figures 1G and 1H), indicating a faster recovery from the bladder areflexia period typically seen after SCI. These data show that the spiny mouse is an outstanding exception to other adult mammals evaluated so far, being capable of spontaneous, robust, and fast restoration of function after severe CNS injury.

The *Acomys* SCI site shows robust axon regeneration of multiple tracts, synapse formation, and signal propagation

For an in-depth comprehension of *Acomys* CNS regeneration, we first examined whether there were any anatomical or structural differences between the spinal cords of *Mus* and *Acomys*. Although *Acomys* (weight, 30–40 g) has a 1.3-fold larger cross section area of the spinal cord than *Mus* (weight, 20–30 g), no main differences in its anatomical organization (Figure S1A) and white/gray matter ratio were found (Figure S1B). We then analyzed the injured spinal cord from both genera. Unlike *Mus*, in which the scar tissue does not respect the original tissue borders, the injured *Acomys* spinal cord established a bridging tissue connecting the rostral and caudal boundaries of the lesion site (Figure 2A), thus providing a unique structural continuity of the initial spinal cord geometry. Eight WPI, *Mus* scar was mostly devoid of β III-tubulin-positive axons and these were only found retracted in relation to the injury area (Figure 2B). Notably, *Acomys* presented a wound densely filled with β III-tubulin-positive axons penetrating and spanning the new bridging tissue (Figure 2B), exhibiting a significantly increased number of regenerating axons in comparison with *Mus*, in which axon growth is strictly limited to the border lesion (Figure 2C). Importantly, some of the axons crossing the lesion site in *Acomys* were already myelinated (Figure 2D), indicating the execution of a complete regenerative program encompassing myelination.

When assessing regeneration of individual axon tracts, we found that superior cervical ganglion 10 (SCG10)-positive

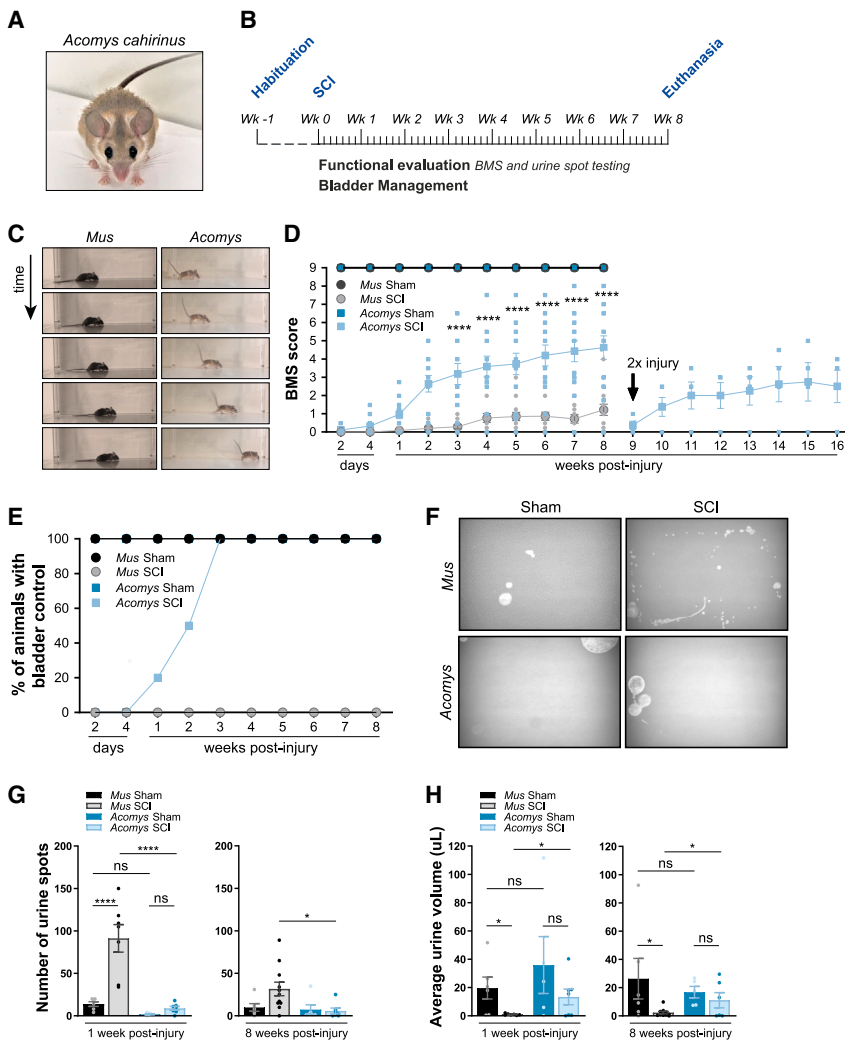


Figure 1. *Acomys* spontaneously recovers function following complete spinal cord transection

(A) Image of an *Acomys cahirinus*.
 (B) Timeline of the experimental setup. Both species were maintained for 8 WPI for weekly functional analysis.
 (C) Sequential images (1 s) of *Mus* and *Acomys* at 8 WPI.
 (D) Assessment of motor function in sham and injured *Mus* and *Acomys* using BMS, showing the average score of left and right hind limbs. Data represent mean \pm SEM (**** $p < 0.0001$ injured *Mus* versus injured *Acomys*, two-way ANOVA followed by Tukey's multiple comparison test); $n = 5$ sham *Mus*, $n = 14$ injured *Mus*, $n = 5$ sham *Acomys*, and $n = 14$ injured *Acomys* until 8 WPI and $n = 4$ injured *Acomys* until 16 WPI, that underwent a second lesion (2 \times lesion).
 (E) Percentage of animals recovering bladder control in both genera ($n = 4$ sham *Mus*, $n = 11$ injured *Mus*, $n = 4$ sham *Acomys*, and $n = 9$ injured *Acomys*).
 (F) Representative images of the urine spots of *Mus* (upper) and *Acomys* (lower).
 (G) Number of voided urine spots. Data represent mean \pm SEM (ns: not significant, * $p < 0.05$, **** $p < 0.0001$, one-way ANOVA followed by Tukey's multiple comparison test and Kruskal-Wallis followed by Dunn's multiple comparisons test). At 1 WPI $n = 6$ sham *Mus*, $n = 7$ injured *Mus*, $n = 5$ sham *Acomys*, and $n = 7$ injured *Acomys*; at 8 WPI $n = 6$ sham *Mus*, $n = 11$ injured *Mus*, $n = 6$ sham *Acomys*, and $n = 7$ injured *Acomys*.
 (H) Average volume of voided urine spots. Data represent mean \pm SEM (ns, not significant, * $p < 0.05$, two-tailed unpaired t test). At 1 WPI $n = 6$ sham *Mus*, $n = 7$ injured *Mus*, $n = 5$ sham *Acomys*, and $n = 7$ injured *Acomys*; at 8 WPI $n = 6$ sham *Mus*, $n = 11$ injured *Mus*, $n = 5$ sham *Acomys*, and $n = 6$ injured *Acomys*.
 Each data point in (D, G, and H) represents values of single animals. See also Videos S1 and S2.

sensory axons penetrated the bridging tissue in injured *Acomys* but were accumulated at the caudal border of the injury in *Mus* (Figure 2E). Additionally, descending serotonin (5-HT) containing axons from the motor raphespinal tract regenerated through the lesion in *Acomys* spinal cord (Figures 2F and S1C). While no differences in 5-HT-immunoreactivity were detected rostrally to the lesion in *Acomys* and *Mus*, the former showed stronger 5-HT staining caudally to the injury site (Figure S1D). In sagittal spinal cord sections, 5-HT-positive axons regenerated extensively through the lesion border, growing for large distances in *Acomys*, whereas these axons mostly accumulated at the lesion edge in *Mus* (Figures 2F–2H). Of note, similarly to humans and unlike *Mus*, cysts were observed in the vicinity of the lesion site of *Acomys* (Figure 2F, highlighted by an asterisk). The corticospinal tract (CST)—the major descending tract involved in voluntary motor function—was traced by intracortical AAV1/2-eGFP injection at 8 WPI (Figure 2I). In cross sections, the CST runs in the ventral part of the posterior funiculus in both *Mus* and *Acomys* (Figures 2I' and 2I''', highlighted by white arrowheads). In *Acomys*, in contrast to *Mus*, bilateral axon sprouting was found caudally to the injury site at 12 WPI (Figure 2I'''). In

injured *Acomys*, CST axons developed a peculiar pattern of axon arborizations with numerous ventrally directed collaterals caudally to the lesion site (Figure 2J).

In *Acomys*, re-establishment of synaptic connectivity was evidenced by the presence of the pre-synaptic vesicular glutamate transporter 1 (vGlut1)-positive/eGFP-positive buttons caudally to injury site following AAV injection (Figure 2K), thus indicating formation of synapses. Although the density of vGlut1+ synaptic boutons on eGFP+ axons was low, as expected from the fact that intracortical AAV1/2-eGFP injection transduces a limited number of neurons, no eGFP+/vGlut1+ axons were found in *Mus* (not shown). To study conduction of compound action potentials (CAPs) in descending motor tracts, the lateral funiculus was stimulated (Figure 2L). No difference was found in the CAP amplitude for uninjured *Mus* and *Acomys* (Figures 2M and 2N). Injured *Acomys* spinal cords (5 out of 10 animals) could conduct CAPs through the lesion site (Figures 2M and 2N). In contrast, no signal conduction across the lesion was detected in *Mus*, as expected from the absence of functional recovery (Figures 2M and 2N). In summary, upon complete SCI, *Acomys* exhibits robust axon regeneration in several

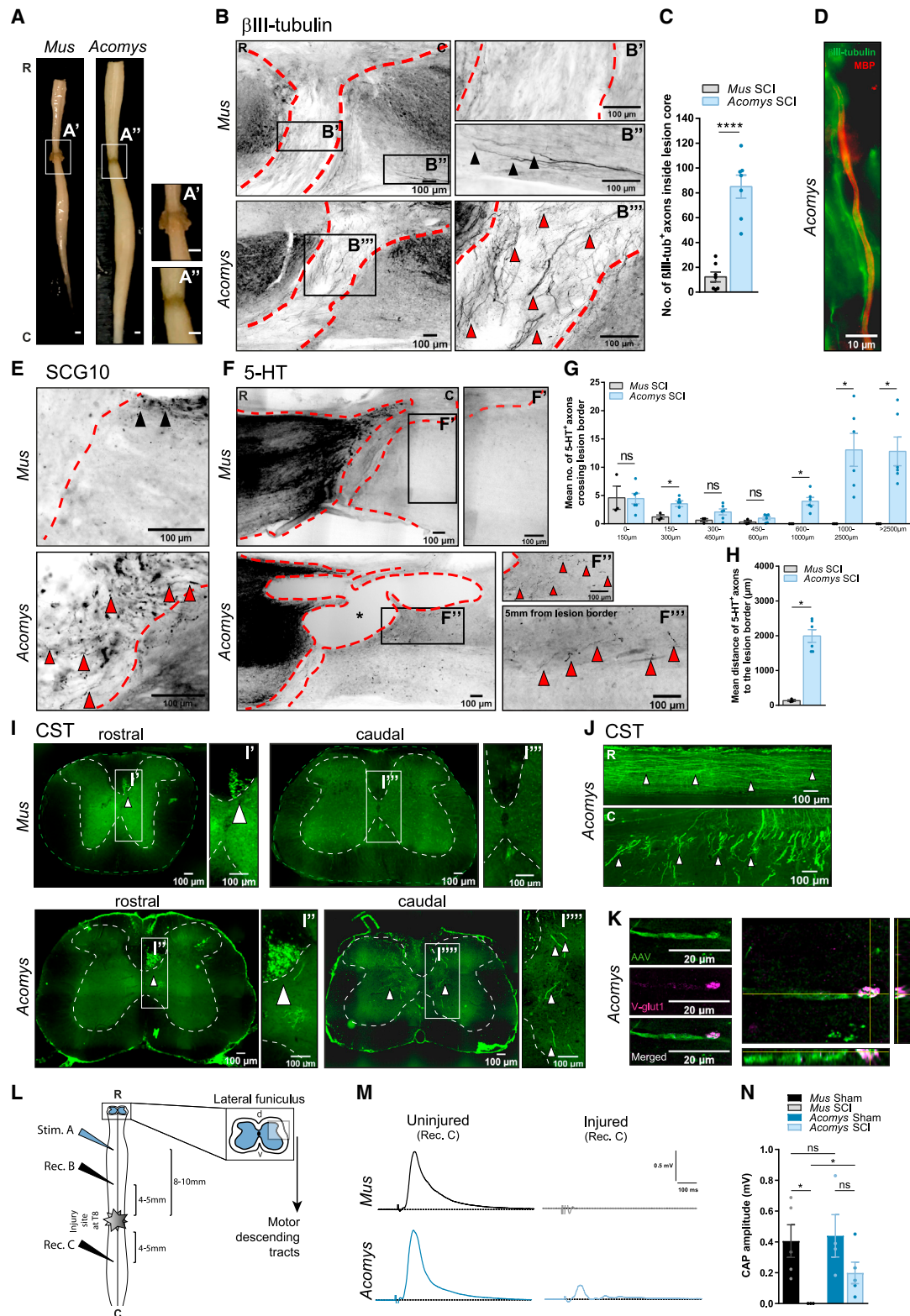


Figure 2. Injured *Acomys* exhibits robust axon regeneration

(A) Representative images of injured *Mus* and *Acomys* spinal cords at 8 WPI. The injury site is boxed in white. The lesion site of *Mus* and *Acomys* is shown at higher magnification in (A' and A''), respectively.

(legend continued on next page)

tracts, synapse formation, and efficient signal propagation throughout the lesion.

After SCI, rewired glycosylation activity is a feature of the *Acomys* spinal cord

The environment created at the injury site is of paramount importance to dictate the success of axon regeneration (Cregg et al., 2014). Given that, we explored the molecular differences that enable *Acomys* to build a scarless injury site. In both genera, astrogliosis was present (Figure S2A). Pan-reactive astrocytes as assessed by GFAP and Ngal/Lcn2 immunofluorescence levels were decreased in *Acomys* (Figures S2B and S2C), supporting a weakened reactive profile. However, no significant differences in A1 astrocytes (generally inferred as detrimental for regeneration, Liddelwold and Barres, 2017; Liddelwold et al., 2017) and A2 astrocytes (commonly considered as neuroprotective and pro-regenerative, Liddelwold and Barres, 2017; Liddelwold et al., 2017) were observed between *Mus* and *Acomys*, as evaluated by the expression levels of different markers of the two subpopulations in the spinal cord (Figure S2D). Similar to the skin and ear (Gawriluk et al., 2016; Matias Santos et al., 2016; Seifert et al., 2012), *Acomys* spinal cords exhibited reduced fibrosis with lower total collagen deposition when compared with *Mus* in which fibrotic scarring was detected (blue staining) (Figure S2E). Specifically, *Mus* showed overt collagen type I deposition throughout the spinal cord parenchyma whereas in injured *Acomys*, it was restricted to the injury site (Figures S2F and S2G). Of note, when comparing the content of pericytes in the lesion core of *Mus* and *Acomys*, no differences were detected as assessed by PDGFR β immunostaining (data not shown).

To further understand the molecular features of the unique scarless environment formed upon SCI in *Acomys*, next-generation sequencing of RNA isolated from the injury site was conducted to identify global differences in gene expression between genus (Table S1), following reconstruction of the *Acomys cahirinus* transcriptome. From the 213 genes expressed in both

genera, grouped in 11 clusters based on their expression pattern similarities (Figure S3), RNA-seq transcriptome analysis showed differential gene expression between uninjured and injured *Mus* and *Acomys* (Figure 3A). PANTHER analysis revealed the involvement of two major functional categories: inflammation-related pathways and acetylglucosaminyltransferase activity (Figures 3B and 3C). As previously reported in other tissues (Gawriluk et al., 2020; Simkin et al., 2017), inflammation was differentially regulated after injury in *Acomys* (Figure 3B). Notably, aside from the immune system, PANTHER analysis also unveiled a SCI-specific alteration in acetylglucosaminyltransferase activity categories (Figure 3C). The *Acomys* injury site exhibited considerable changes in the levels of key enzymes of the biosynthetic pathways of major ECM glycosaminoglycans namely keratan (KSPG) and heparan (HSPG) sulfate proteoglycans (Figures 3A and 3C).

β -1,3-N-acetylglucosaminyltransferase 7 (*β 3gnt7*), a crucial enzyme for KSPG synthesis, was highly increased in injured *Acomys* (Figures 3A and 3C), as validated by qPCR (Figure 3D) and immunofluorescence (Figures 3H and 3I). N-deacetylase-N-sulfotransferase 3 and 4 (*Ndst3* and *Ndst4*), which participate in HSPG post-synthesis modifications (Jao et al., 2016; Pallerla et al., 2008), showed decreased levels in *Acomys* (Figures 3A, 3C, 3E, 3F, 3J, and 3K). PANTHER analysis additionally identified β -1,3-N-acetylgalactosaminyltransferase 1 (*β 3galnt1*), also from cluster 6, that participates in the biosynthesis of glycosphingolipids, as decreased in *Acomys* upon injury (Figures 3A, 3C, and 3G). PANTHER analysis also included phosphoglucomutase 5 (*Pgm5*) and β -1,3-N-acetylglucosaminyltransferase (*Mfng*) within the carbohydrate biosynthetic process/acetylglucosaminyltransferase categories (Figures 3A and 3C). However, *Pgm5* has been reported as lacking enzymatic activity (Muenks et al., 2017), whereas *Mfng* activity is involved in Notch modification and regulation (Kakuda and Haltiwanger, 2017). These genes were therefore not considered for further analysis in the context of the current study.

(B) Sagittal spinal cord sections encompassing the lesion core immunostained with β III-tubulin of *Mus* (upper) and *Acomys* (lower) at 8 WPI. Black arrowheads in (B^{''}) indicate *Mus* axons interrupted caudally to the injury border; red arrowheads in (B^{'''}) indicate *Acomys* axons growing within the injury site.

(C) Number of β III-tubulin-positive axons regenerating within the injury site related to (B). Data represent mean \pm SEM (****p < 0.0001, two-tailed unpaired t test) of n = 7 injured *Mus* and n = 7 injured *Acomys*.

(D) *Acomys* spinal cord lesion core stained with β III-tubulin (green) and myelin-basic protein (MBP) (red) at 8 WPI.

(E) Sagittal spinal cord sections encompassing the lesion core immunostained with SCG10 of *Mus* (upper) and *Acomys* (lower) at 8 WPI. Black arrowheads indicate *Mus* axons arrested at the lesion border and red arrowheads indicate *Acomys* axons penetrating the lesion.

(F) Sagittal spinal cord sections encompassing the lesion core immunostained with 5-HT of *Mus* (upper) and *Acomys* (lower) at 8 WPI. Red arrowheads in (F^{''}) and (F^{'''}) highlight *Acomys* axons regenerating caudally to injury. A cyst *Acomys* is highlighted by an asterisk in (F).

(G) Mean number of 5-HT-positive axons protruding for different distances beyond the lesion border related to (F). Data represent mean \pm SEM (*p < 0.05, **p < 0.01, two-tailed Mann-Whitney test, ns: not significant) of n = 3 injured *Mus* and n = 6 injured *Acomys*.

(H) Mean distance of 5-HT-positive axons protruding beyond the lesion border related to (F). Data represent mean \pm SEM (*p < 0.05, two-tailed Mann-Whitney test) of n = 3 injured *Mus* and n = 6 injured *Acomys*.

(I) Transverse spinal cord section of injured *Mus* and *Acomys* spinal cord showing eGFP expression at 12 WPI. White arrowheads in (I[']) and (I^{''}) highlight the CST running in the ventral part of the posterior funiculus in both *Mus* and *Acomys* and in (I^{'''}) regenerating CST fibers.

(J) Sagittal spinal cord sections of an injured *Acomys* spinal cord showing CST axons labeled by eGFP expression at 12 WPI. White arrowheads highlight CST axons rostrally (R, upper panel) and caudally (C, lower panel) to the lesion site.

(K) Pre-synaptic vGlut1 marker staining (magenta) of regenerating axons in injured AAV1/2-eGFP-injected *Acomys* at 12 WPI.

(L) Scheme of the experimental setup to measure CAP conduction in the lateral funiculus.

(M) CAP conduction of the uninjured and injured *Mus* and *Acomys* spinal cords at 8 WPI.

(N) Quantification related to (M). Data represent mean \pm SEM (*p < 0.05, two-tailed Mann-Whitney test; n.s., non-significant); n = 5 sham *Mus*, n = 3 injured *Mus*, n = 4 sham *Acomys*, and n = 5 injured *Acomys*.

Each data point in (C, G, H, and N) represents values of single animals. Zoom-ins of regions of interest are provided at the right side of each image. Dashed red lines in (B, E, and F) define lesion borders. Dashed white line in (I) define spinal cord gray matter border. Scale bars: 1 mm in (A), 10 μ m in (D), 20 μ m in (K), and 100 μ m in (B, E, F, I, and J). R, rostral; C, caudal. See also Figure S1.

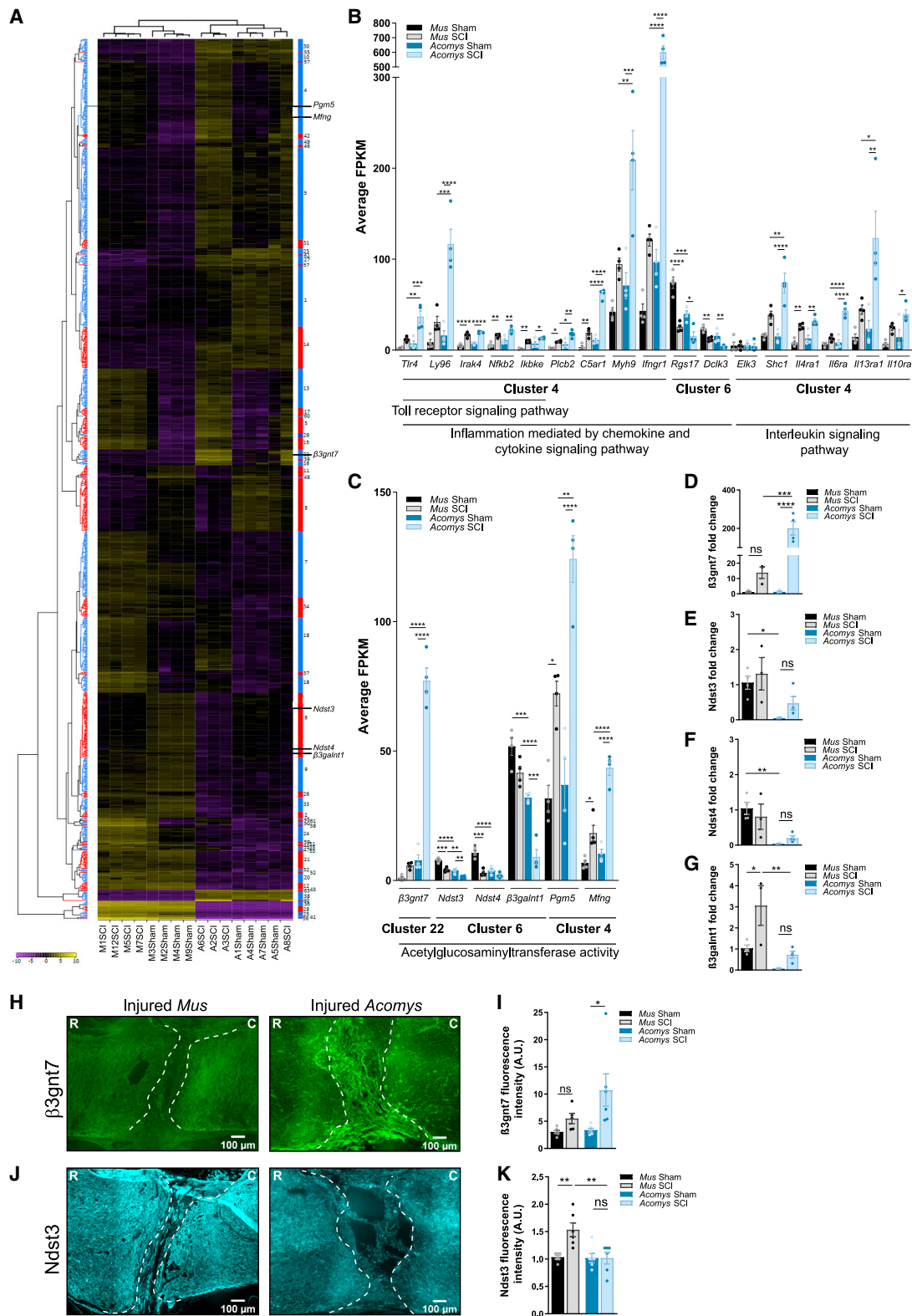


Figure 3. After SCI, rewired glycosyltransferase activity is a feature of the *Acomys* spinal cord

(A) Heatmap of RNA-seq transcriptome analysis showing differentially gene expression between uninjured and injured *Mus* and *Acomys*, by hierarchical cluster analysis. Gene clusters are indicated by numbers, and genes within the clusters are alternately shown in blue and red.

(legend continued on next page)

When we further examined differentially expressed genes, other enzymes including carbohydrate sulfotransferases that participate in the biosynthesis of other ECM glycosaminoglycan such as chondroitin sulfate proteoglycans (CSPGs) were differentially regulated in *Acomys* (Figure S4A). The glycosaminoglycan chains of CSPGs are mainly sulfated in the 4 (C4) or 6 (C6) positions. While C4S appears to be inhibitory for axonal growth, C6S can positively affect regeneration and plasticity (Lin et al., 2011; Miller and Hsieh-Wilson, 2015; Wang et al., 2008). No significant differences were found on expression levels of major C4S-sulfotransferases; however, injured *Acomys* exhibits a large increase in C6S-sulfotransferase *Chst15* expression (Figure S4A). Although no main gene expression alterations were detected in the levels of known inhibitory CSPGs such as aggrecan, neurocan, versican, or brevican between *Mus* and *Acomys* (not shown), the increase in *Chst15* expression may provide a more permissive environment for axon growth. Alterations on the expression of these genes reinforces a major rewiring of glycosyltransferase biosynthetic pathways to ensure the regenerative response of *Acomys*.

***Acomys* exhibits a specific proteoglycan signature at the lesion site where $\beta 3gnt7$ acts as an axon growth enhancer**

Given that $\beta 3gnt7$ expression is highly increased in the *Acomys* spinal cord following injury (Figures 3C, 3D, 3G, and 3H), and its essential role in KSPG synthesis, we further investigated the consequences of $\beta 3gnt7$ differential regulation in KSPG deposition. After injury, *Acomys* exhibited a robust over 30-fold increased KSPG deposition that extended rostrally and caudally to the lesion site, and that was reverted by keratanase treatment (Figures 4A and 4B). Changes in proteoglycan deposition were not limited to KSPG, as decreased deposition of HSPG was also observed (Figures 4C and 4D), in accordance with the decreased levels of *Ndst3* and *Ndst4* (Figures 3E and 3F). HSPG staining was reverted by heparinase treatment, demonstrating the specificity of analysis (Figures 4C and 4D).

To interrogate the role of $\beta 3gnt7$ in the settings of axon growth, we used similar assays to those previously developed by the Filbin group to identify novel regulators of axon regeneration (Mukhopadhyay et al., 1994). For that, Chinese Hamster Ovary (CHO) cells overexpressing $\beta 3gnt7$ (i.e., modified in an *Acomys*-like manner) were used as a substrate to grow *Mus* DRG and cortical neurons (Figures 4E and 4I). *Mus* DRG neurons

had a very robust increased total neurite length (Figures 4F–4H) when exposed to cells overexpressing $\beta 3gnt7$. Similarly, *Mus* cortical neurons exhibited an increased axon growth capacity in the presence of high $\beta 3gnt7$ levels, which was already observed at an early time point (1 day) after plating (Figure 4I). These data support that $\beta 3gnt7$ is a target to increase axon regeneration after SCI. In summary, our data reveal a unique transcriptional program in *Acomys*, in which differential immune response and rewired acetylglucosaminyltransferase activity culminate in the assembly of a regeneration supportive scarless injury site, and identifies $\beta 3gnt7$, a critical enzyme in KSPG biosynthesis, as an enhancer of axon growth.

DISCUSSION

The ability to restore functional organs upon damage, including the spinal cord, occurs in several non-mammalian vertebrates such as fish and reptiles but is extremely restricted or non-existent in adult mammals (Diaz Quiroz and Echeverri, 2013; Lee-Liu et al., 2013). As such, to date, despite the efforts to promote functional axon regeneration in the adult mammalian CNS, SCI treatments remain largely palliative. Here, we reveal that *Acomys*, a mammal closely related to *Mus*, can spontaneously regenerate after SCI, overturning the established dogma. This discovery sets *Acomys* as a unique model to investigate mammalian CNS regeneration and allowed us to start interrogating the mechanisms required to sustain axon regrowth in adult mammals.

One of the first consequences of tissue injury is inflammation (Oishi and Manabe, 2018). In *Acomys*, part of the receptor complex for a major pro-inflammatory cytokine, interferon gamma (IFN- γ) (Wu et al., 2014), is increased after injury. However, the high expression levels of *ifngr1* cannot be taken as evidence for an ongoing pro-inflammatory response. Of note, the active IFN- γ receptor is made of two *ifngr1* and two *ifngr2* chains (Randal and Kossiakoff, 2001), and only *ifngr1* expression is highly increased in *Acomys* after SCI. In fact, *ifngr2* expression is lower in *Acomys* than in *Mus* (Table S1). Furthermore, the upregulation of the receptors for the major anti-inflammatory cytokines supports that an anti-inflammatory response might be underway at the *Acomys* lesion site, as is seen in other tissues (Gawriluk et al., 2020; Simkin et al., 2017) warranting further investigation.

High-throughput analysis of the extracellular proteome in rats has supported the importance of inflammation and ECM

(B and C) Average fragments per kilobase of transcript per million mapped reads (FPKM) values obtained by transcriptomic analysis of categories identified by PANTHER. (B) Inflammation-related pathways and (C) acetylglucosaminyltransferase activity categories, from clusters 4, 6, and 22, detected from the 11 Trinity gene clusters analyzed. Only clusters for which more than 75% of the members show a statistically significant difference were analyzed. Data represent mean \pm SEM (* $p < 0.05$, ** $p < 0.01$, *** $p < 0.001$, **** $p < 0.0001$, one-way ANOVA followed by Tukey's multiple comparison test, ns: not significant) of $n = 4$ sham *Mus*; $n = 4$ injured *Mus*, $n = 4$ sham *Acomys*, and $n = 4$ injured *Acomys*.

(D–G) qPCR results for acetylglucosaminyltransferase-activity-related genes: (D) $\beta 3gnt7$, (E) *Ndst3*, (F) *Ndst4*, and (G) $\beta 3galnt1$. Data represent mean \pm SEM (* $p < 0.05$, ** $p < 0.01$, *** $p < 0.001$, **** $p < 0.0001$, one-way ANOVA followed by Tukey's multiple comparison test, ns: not significant); $n = 4$ sham *Mus*; $n = 3$ injured *Mus*, $n = 4$ sham *Acomys*, and $n = 4$ injured *Acomys*.

(H) Sagittal spinal cord sections containing the injury site of *Mus* and *Acomys* stained for $\beta 3gnt7$ at 8 WPI.

(I) Quantification related to (H). Data represent mean \pm SEM (* $p < 0.05$, one-way ANOVA followed by Tukey's multiple comparison test, ns: not significant); $n = 6$ sham *Mus*, $n = 6$ injured *Mus*, $n = 6$ sham *Acomys* and $n = 6$ injured *Acomys*.

(J) Sagittal spinal cord sections containing the injury site of *Mus* and *Acomys* stained for *Ndst3* at 8 WPI.

(K) Quantification related to (J). Data represent mean \pm SEM (** $p < 0.01$, one-way ANOVA followed by Tukey's multiple comparison test, ns: not significant); $n = 6$ sham *Mus*, $n = 6$ injured *Mus*, $n = 6$ sham *Acomys*, and $n = 6$ injured *Acomys*.

Each data point in (B–G, I, and K) represents values of single animals. Dashed white lines in (H and J) define lesion borders. Scale bars, 100 μ m (H and J). R: rostral; C: caudal. See also Table S1 and Figures S2–S4.

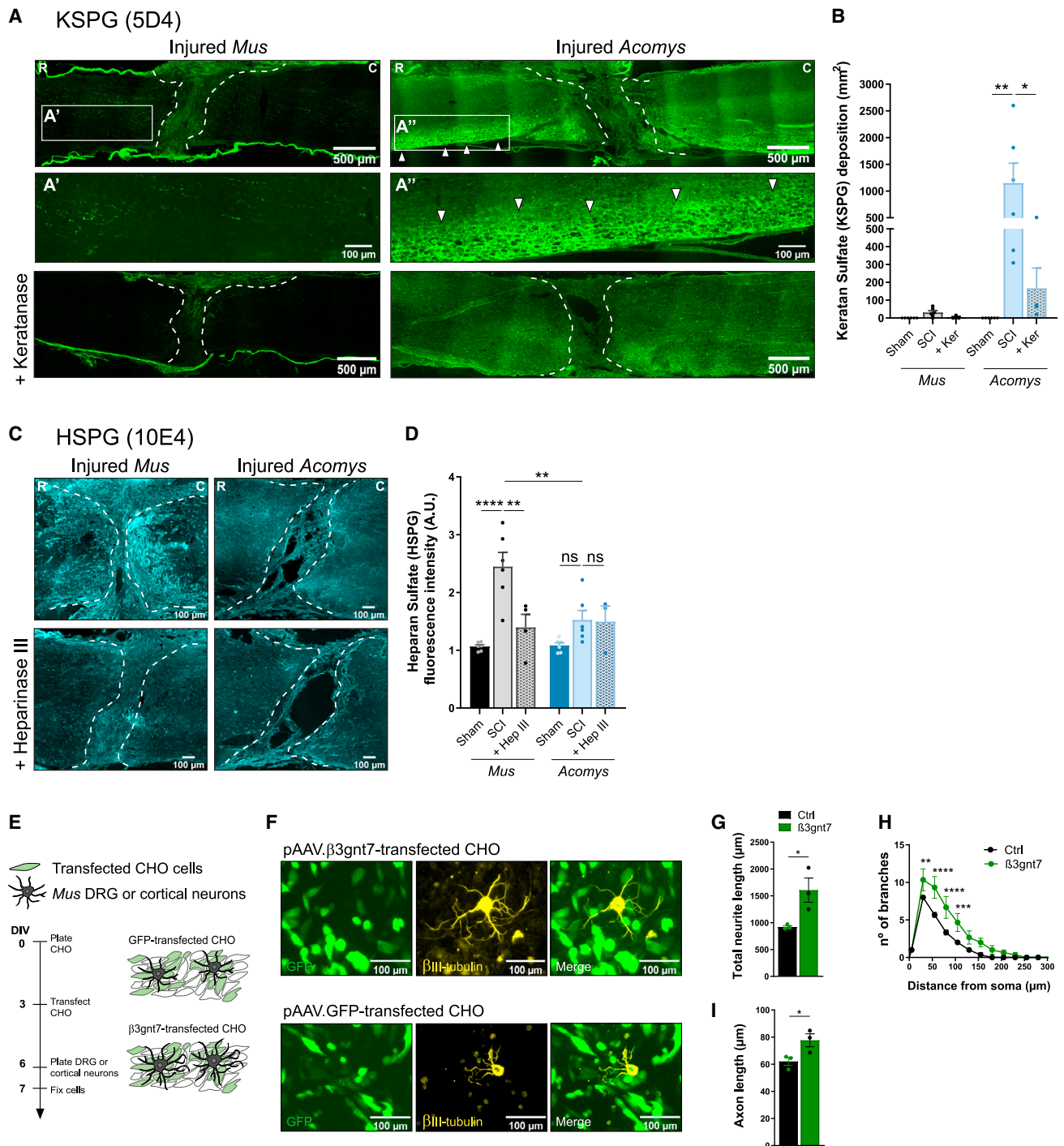


Figure 4. *Acomys* exhibits a specific proteoglycan signature at the lesion site where β 3gnt7 acts as an axon growth enhancer

(A) Sagittal spinal cord sections encompassing the lesion core of injured *Mus* (left) and *Acomys* (right) stained for KSPG (5D4) and digested with keratanase at 8 WPI. Zoom-ins of regions of interest are provided in lower panels in (A') and (A''). White arrowheads in (A'') highlight KSPG deposition with honeycomb-like shape throughout the injured *Acomys* spinal cord.

(B) Quantification of KSPG area of deposition related to (A). Data represent mean \pm SEM (* p < 0.05, ** p < 0.01, two-tailed Mann-Whitney test); n = 6 sham *Mus*, n = 6 injured *Mus*, n = 4 injured *Mus* with keratanase treatment, n = 6 sham *Acomys*, n = 6 injured *Acomys*, and n = 4 injured *Acomys* with keratanase treatment.

(C) Sagittal spinal cord sections encompassing the lesion core of injured *Mus* (left) and *Acomys* (right) stained for HSPG (10E4) and digested with heparinase III at 8 WPI.

(D) Quantification of HSPG fluorescence intensity at the lesion site related to (A). Data represent mean \pm SEM (** p < 0.01, *** p < 0.001, and **** p < 0.0001, one-way ANOVA followed by Tukey's multiple comparison test, ns: not significant); n = 6 sham *Mus*, n = 6 injured *Mus*, n = 4 injured *Mus* with heparinase III treatment, n = 6 sham *Acomys*, n = 6 injured *Acomys*, and n = 4 injured *Acomys* with heparinase III treatment.

(legend continued on next page)

composition in the response mounted upon SCI (Didangelos et al., 2016). Studies comparing non-regenerative and regenerative non-mammalian species after SCI, including the axolotl (Tica and Didangelos, 2018) and zebrafish (Tsata et al., 2021) have further pinpointed inflammation and ECM components as critical factors in interspecies regenerative differences. Similar to *Acomys*, in zebrafish, the deposition of a growth-supporting ECM deprived of growth inhibitory matrix molecules is crucial for axon regeneration after SCI (Tsata et al., 2021). Furthermore, in zebrafish, a regenerative permissive milieu is enabled by the recruitment of pdgfrb+ myoseptal and perivascular cells, in a PDGFR signaling-dependent manner (Tsata et al., 2021). In *Acomys*, we unveiled the glycosylation gene regulatory network as a key spinal cord-specific pathway that differentiates the *Acomys* and *Mus* lesion environment. In fact, injured *Acomys* exhibits a specific signature of ECM glycosaminoglycans at the SCI site. Although previous studies reported the potential role of KSPG as an inhibitor of axon regeneration (Imagama et al., 2011; Ishikawa et al., 2015; Jones and Tuszyński, 2002), here, we show that in fact KSPG glycosaminoglycan chains are increased in the pro-regenerative environment of the *Acomys* lesion site. Moreover, we identify $\beta 3gnt7$, a crucial enzyme in KSPG biosynthesis, as a potent enhancer of axon growth, which may be explored in the future design of therapies to enhance axon regeneration after SCI.

Taken together, our data establish that the *Acomys* acetylglucosaminyltransferase gene regulatory network has distinctive and exclusive features that reprograms the *Acomys* ECM after SCI, being able to give rise to an effective pro-regenerative wounding response. Our results underscore the importance of investigating regenerative phenomena outside traditional model organisms and suggest that some mammals may retain a sophisticated capacity for CNS regeneration. This fundamental knowledge on pathways required for axon regrowth in adult mammals may ultimately be used with the final goal of devising novel therapeutic applications for human CNS injury.

Limitations of the study

(1) Retrograde tracing: long-distance axon tracing was only performed anterogradely; retrograde tracing to identify the soma of the axon in regrown axonal tracts could be performed in the future. (2) Analysis of CSPG deposition: in this study, we opted to focus on KSPG and HSPG deposition, as the *Acomys* injury site exhibited considerable changes specifically in the levels of key enzymes of the biosynthetic pathways of these proteoglycans. Future work will examine levels of deposition of CSPG, sulfated either in 4-O position of the GalNAc residue (thought to be inhibitory for axon growth) or 6-O position (permissive for axon growth). (3) *In vivo* assays: we show that after SCI, *Acomys* has increased levels of $\beta 3gnt7$, a crucial enzyme of KSPG biosynthesis, and increased KSPG deposition in the spinal cord. We additionally demonstrate

that *in vitro* $\beta 3gnt7$ is an enhancer of axon growth. Given these findings, it would be of great interest to perform the *in vivo* overexpression of $\beta 3gnt7$ in *Mus*, to determine if $\beta 3gnt7$ is sufficient to dictate significant axon regeneration after SCI in a non-regenerative species. Furthermore, downregulation of $\beta 3gnt7$ in injured *Acomys* and investigation of subsequent axon regeneration would further define the role and importance of this specific KSPG synthetic enzyme in *Acomys* spinal cord regeneration. It would also be of interest to analyze the effect of keratanase treatment on axon regeneration of *Acomys*. This would allow to further validate the role of KSPG deposition in contributing to a regeneration-promoting environment.

STAR★METHODS

Detailed methods are provided in the online version of this paper and include the following:

- KEY RESOURCES TABLE
- RESOURCE AVAILABILITY
 - Lead contact
 - Materials availability
 - Data and code availability
- EXPERIMENTAL MODELS AND SUBJECT DETAILS
 - Animals
 - Cell lines
 - Primary cultures
- METHOD DETAILS
 - Spinal cord injury and post-surgical animal care
 - Functional evaluation
 - Histology and immunofluorescence analysis
 - AAV injection for anterograde tracing
 - Electrophysiology
 - RNA extraction and transcriptomic analysis
 - Neurite outgrowth assay
- QUANTIFICATION AND STATISTICAL ANALYSIS

SUPPLEMENTAL INFORMATION

Supplemental information can be found online at <https://doi.org/10.1016/j.devcel.2021.12.008>.

ACKNOWLEDGMENTS

We thank the i3S Scientific Platforms (Animal, Histology and Electron Microscopy, Advanced Light Microscopy and BioSciences Screening Facilities, part of the national infrastructure Portuguese Platform of Biomaging [PPBI]; PPBI-POCI-01-0145-FEDER-022122). This project was supported by Santa Casa da Misericórdia de Lisboa (MC-39-2019), Wings for Life (WFL-PT-21/20), FCT (UID/BIM/04773/2013/CBMR, PTDC/BIA-ANM/0697/2014, PTDC/MED-ONC/28489/2017). J.N.R. and S.C.S. are FCT fellows (SFRH/BD/131565/2017; SFRH/BD/136760/2018).

(E) Scheme of the experimental setup of co-culture of transfected CHO cells and *Mus* DRG or cortical neurons.

(F) β III-tubulin staining (yellow) of *Mus* DRG neurons plated on top of GFP-transfected or $\beta 3gnt7$ -GFP-transfected CHO cells (green).

(G and H) Total neurite length (G) and branching analysis (H) of *Mus* DRG neurons grown on top of transfected CHO cells related to (F). Data represent mean \pm SEM (* $p < 0.05$, two-tailed unpaired t test) of 3 independent experiments (52–104 neurons analyzed in each experiment).

(I) Axon length of *Mus* cortical neurons grown on top of transfected CHO cells. Data represent mean \pm SEM (* $p < 0.05$, two-tailed unpaired t test) of 3 independent experiments (73–287 neurons analyzed in each experiment).

Dashed white lines in (A and C) define lesion borders. Each data point in (B and D) represents values of single animals. Each data point in (G and I) represents values of independent experiments. Scale bars, 100 μ m (A, C, F, and J). R: rostral; C: caudal.

AUTHOR CONTRIBUTIONS

M.M.S. coordinated the study; G.T. and I.M.A. coordinated research at University of Algarve; M.M.S., J.N.-R., C.D.C., B.V.S., A.M., and C.R. designed and analyzed experiments; J.N.R., S.C.L., R.P.-C., S.C.S., L.L.L., M.A.S., R.O., and A.C.M. performed experiments and quantifications; G.G.P., M.V., J.A.S., S.S., and V.E.F. supported preliminary experiments in *Acomys*; V.B. and J.P. performed RNA-seq experiments; C.P.V. and J.V. performed RNA-seq analyzes and their interpretation; M.M.S. and J.N.R. wrote the paper with input from all authors.

DECLARATION OF INTERESTS

The authors declare no competing interests.

Received: March 26, 2021

Revised: November 26, 2021

Accepted: December 8, 2021

Published: January 4, 2022

REFERENCES

- Basso, D.M., Fisher, L.C., Anderson, A.J., Jakeman, L.B., McTigue, D.M., and Popovich, P.G. (2006). Basso mouse scale for locomotion detects differences in recovery after spinal cord injury in five common mouse strains. *J. Neurotrauma* 23, 635–659. <https://doi.org/10.1089/neu.2006.23.635>.
- Brant, J.O., Lopez, M.C., Baker, H.V., Barbazuk, W.B., and Maden, M. (2015). A comparative analysis of gene expression profiles during skin regeneration in *Mus* and *Acomys*. *PLoS One* 10, e0142931. <https://doi.org/10.1371/journal.pone.0142931>.
- Brant, J.O., Yoon, J.H., Polvadore, T., Barbazuk, W.B., and Maden, M. (2016). Cellular events during scar-free skin regeneration in the spiny mouse, *Acomys*. *Wound Repair Regen* 24, 75–88. <https://doi.org/10.1111/wrr.12385>.
- Chen, H., Zhang, L., Hill, W.G., and Yu, W. (2017). Evaluating the voiding spot assay in mice: a simple method with complex environmental interactions. *Am. J. Physiol. Renal Physiol.* 313, F1274–F1280. <https://doi.org/10.1152/ajprenal.00318.2017>.
- Cregg, J.M., DePaul, M.A., Filous, A.R., Lang, B.T., Tran, A., and Silver, J. (2014). Functional regeneration beyond the glial scar. *Exp. Neurol.* 253, 197–207. <https://doi.org/10.1016/j.expneurol.2013.12.024>.
- Cyr, J.L., Gawriluk, T.R., Kimani, J.M., Rada, B., Watford, W.T., Kiama, S.G., Seifert, A.W., and Ezenwa, V.O. (2019). Regeneration-competent and -incompetent murids differ in neutrophil quantity and function. *Integr. Comp. Biol.* 59, 1138–1149. <https://doi.org/10.1093/icb/icz023>.
- Dent, E.W., Callaway, J.L., Szebenyi, G., Baas, P.W., and Kalil, K. (1999). Reorganization and movement of microtubules in axonal growth cones and developing interstitial branches. *J. Neurosci.* 19, 8894–8908.
- Dias, D.O., and Göritz, C. (2018). Fibrotic scarring following lesions to the central nervous system. *Matrix Biol* 68 (69), 561–570. <https://doi.org/10.1016/j.matbio.2018.02.009>.
- Diaz Quiroz, J.F., and Echeverri, K. (2013). Spinal cord regeneration: where fish, frogs and salamanders lead the way, can we follow? *Biochem. J.* 451, 353–364. <https://doi.org/10.1042/BJJ20121807>.
- Didangelos, A., Puglia, M., Iberl, M., Sanchez-Bellot, C., Roschitzki, B., and Bradbury, E.J. (2016). High-throughput proteomics reveal alarmins as amplifiers of tissue pathology and inflammation after spinal cord injury. *Sci. Rep.* 6, 21607. <https://doi.org/10.1038/srep21607>.
- Du, K., Zheng, S., Zhang, Q., Li, S., Gao, X., Wang, J., Jiang, L., and Liu, K. (2015). Pten deletion promotes regrowth of corticospinal tract axons 1 year after spinal cord injury. *J. Neurosci.* 35, 9754–9763. <https://doi.org/10.1523/JNEUROSCI.3637-14.2015>.
- Gawriluk, T.R., Simkin, J., Hacker, C.K., Kimani, J.M., Kiama, S.G., Ezenwa, V.O., and Seifert, A.W. (2020). Complex tissue regeneration in mammals is associated with reduced inflammatory cytokines and an influx of T cells. *Front. Immunol.* 11, 1695. <https://doi.org/10.3389/fimmu.2020.01695>.
- Gawriluk, T.R., Simkin, J., Thompson, K.L., Biswas, S.K., Clare-Salzler, Z., Kimani, J.M., Kiama, S.G., Smith, J.J., Ezenwa, V.O., and Seifert, A.W. (2016). Comparative analysis of ear-hole closure identifies epimorphic regeneration as a discrete trait in mammals. *Nat. Commun.* 7, 11164. <https://doi.org/10.1038/ncomms11164>.
- Giger, R.J., Hollis, E.R., 2nd, and Tuszynski, M.H. (2010). Guidance molecules in axon regeneration. *Cold Spring Harb. Perspect. Biol.* 2, a001867. <https://doi.org/10.1101/cshperspect.a001867>.
- Haas, B.J., Papanicolaou, A., Yassour, M., Grabherr, M., Blood, P.D., Bowden, J., Couger, M.B., Eccles, D., Li, B., Lieber, M., et al. (2013). *De novo* transcript sequence reconstruction from RNA-seq using the Trinity platform for reference generation and analysis. *Nat. Protoc.* 8, 1494–1512. <https://doi.org/10.1038/nprot.2013.084>.
- Hamid, R., Averbeck, M.A., Chiang, H., Garcia, A., Al Mousa, R.T., Oh, S.J., Patel, A., Plata, M., and Del Popolo, G. (2018). Epidemiology and pathophysiology of neurogenic bladder after spinal cord injury. *World J. Urol.* 36, 1517–1527. <https://doi.org/10.1007/s00345-018-2301-z>.
- Imagama, S., Sakamoto, K., Tauchi, R., Shinjo, R., Ohgomi, T., Ito, Z., Zhang, H., Nishida, Y., Asami, N., Takeshita, S., et al. (2011). Keratan sulfate restricts neural plasticity after spinal cord injury. *J. Neurosci.* 31, 17091–17102. <https://doi.org/10.1523/JNEUROSCI.5120-10.2011>.
- Ishikawa, Y., Imagama, S., Ohgomi, T., Ishiguro, N., and Kadomatsu, K. (2015). A combination of keratan sulfate digestion and rehabilitation promotes anatomical plasticity after rat spinal cord injury. *Neurosci. Lett.* 593, 13–18. <https://doi.org/10.1016/j.neulet.2015.03.015>.
- Jao, T.M., Li, Y.L., Lin, S.W., Tzeng, S.T., Yu, I.S., Yen, S.J., Tsai, M.H., and Yang, Y.C. (2016). Alteration of colonic epithelial cell differentiation in mice deficient for glucosaminyl N-deacetylase/N-sulfotransferase 4. *Oncotarget* 7, 84938–84950. <https://doi.org/10.18632/oncotarget.12915>.
- Jin, D., Liu, Y., Sun, F., Wang, X., Liu, X., and He, Z. (2015). Restoration of skilled locomotion by sprouting corticospinal axons induced by co-deletion of PTEN and SOCS3. *Nat. Commun.* 6, 8074. <https://doi.org/10.1038/ncomms9074>.
- Jones, L.L., and Tuszynski, M.H. (2002). Spinal cord injury elicits expression of keratan sulfate proteoglycans by macrophages, reactive microglia, and oligodendrocyte progenitors. *J. Neurosci.* 22, 4611–4624.
- Kakuda, S., and Haltiwanger, R.S. (2017). Deciphering the Fringe-mediated Notch code: identification of activating and inhibiting sites allowing discrimination between ligands. *Dev. Cell* 40, 193–201. <https://doi.org/10.1016/j.devcel.2016.12.013>.
- Law, C.W., Chen, Y., Shi, W., and Smyth, G.K. (2014). voom: Precision weights unlock linear model analysis tools for RNA-seq read counts. *Genome Biol* 15, R29. <https://doi.org/10.1186/gb-2014-15-2-r29>.
- Lee-Liu, D., Edwards-Faret, G., Tapia, V.S., and Larrain, J. (2013). Spinal cord regeneration: lessons for mammals from non-mammalian vertebrates. *Genesis* 51, 529–544. <https://doi.org/10.1002/dvg.22406>.
- Leite, S.C., Sampaio, P., Sousa, V.F., Nogueira-Rodrigues, J., Pinto-Costa, R., Peters, L.L., Brites, P., and Sousa, M.M. (2016). The actin-binding protein alpha-Adducin is required for maintaining axon diameter. *Cell Rep* 15, 490–498. <https://doi.org/10.1016/j.celrep.2016.03.047>.
- Liddel, S.A., and Barres, B.A. (2017). Reactive astrocytes: production, function, and therapeutic potential. *Immunity* 46, 957–967. <https://doi.org/10.1016/j.immuni.2017.06.006>.
- Liddel, S.A., Guttenplan, K.A., Clarke, L.E., Bennett, F.C., Bohlen, C.J., Schirmer, L., Bennett, M.L., Münch, A.E., Chung, W.S., Peterson, T.C., et al. (2017). Neurotoxic reactive astrocytes are induced by activated microglia. *Nature* 541, 481–487. <https://doi.org/10.1038/nature21029>.
- Lin, R., Rosahl, T.W., Whiting, P.J., Fawcett, J.W., and Kwok, J.C. (2011). 6-sulphated chondroitins have a positive influence on axonal regeneration. *PLoS One* 6, e21499. <https://doi.org/10.1371/journal.pone.0021499>.
- Lopez-Fernandez, H., Duque, P., Vazquez, N., Fdez-Riverola, F., Reboiro-Jato, M., Vieira, C.P., and Vieira, J. (2020). SEDTA: a desktop tool Suite for FASTA files processing. *IEEE/ACM Trans. Comput. Biol. Bioinform.* <https://doi.org/10.1109/TCBB.2020.3040383>.

- Mar, F.M., da Silva, T.F., Morgado, M.M., Rodrigues, L.G., Rodrigues, D., Pereira, M.I.L., Marques, A., Sousa, V.F., Coentro, J., Sá-Miranda, C., et al. (2016). Myelin lipids inhibit axon regeneration following spinal cord injury: a novel perspective for therapy. *Mol. Neurobiol.* 53, 1052–1064. <https://doi.org/10.1007/s12035-014-9072-3>.
- Martin, M. (2011). Cutadapt removes adapter sequences from high-throughput sequencing reads. *EMBnet. j.* 17, 10–12. <https://doi.org/10.14800/ej.17.1.200>.
- Matias Santos, D., Rita, A.M., Casanellas, I., Brito Ova, A., Araújo, I.M., Power, D., and Tiscornia, G. (2016). Ear wound regeneration in the African spiny mouse *Acomys cahirinus*. *Regeneration (Oxf)* 3, 52–61. <https://doi.org/10.1002/reg2.50>.
- Miller, G.M., and Hsieh-Wilson, L.C. (2015). Sugar-dependent modulation of neuronal development, regeneration, and plasticity by chondroitin sulfate proteoglycans. *Exp. Neurol.* 274, 115–125. <https://doi.org/10.1016/j.expneurol.2015.08.015>.
- Morii, H., Shiraiishi-Yamaguchi, Y., and Mori, N. (2006). SCG10, a microtubule destabilizing factor, stimulates the neurite outgrowth by modulating microtubule dynamics in rat hippocampal primary cultured neurons. *J. Neurobiol.* 66, 1101–1114. <https://doi.org/10.1002/neu.20295>.
- Muenks, A.G., Stiers, K.M., and Beamer, L.J. (2017). Sequence-structure relationships, expression profiles, and disease-associated mutations in the paralogs of phosphoglucomutase 1. *PLoS One* 12, e0183563. <https://doi.org/10.1371/journal.pone.0183563>.
- Mukhopadhyay, G., Doherty, P., Walsh, F.S., Crocker, P.R., and Filbin, M.T. (1994). A novel role for myelin-associated glycoprotein as an inhibitor of axonal regeneration. *Neuron* 13, 757–767. [https://doi.org/10.1016/0896-6273\(94\)90042-6](https://doi.org/10.1016/0896-6273(94)90042-6).
- Oishi, Y., and Manabe, I. (2018). Macrophages in inflammation, repair and regeneration. *Int. Immunol.* 30, 511–528. <https://doi.org/10.1093/intimm/dxy054>.
- Okada, S., Hara, M., Kobayakawa, K., Matsumoto, Y., and Nakashima, Y. (2018). Astrocyte reactivity and astrogliosis after spinal cord injury. *Neurosci. Res.* 126, 39–43. <https://doi.org/10.1016/j.neures.2017.10.004>.
- Pallerla, S.R., Lawrence, R., Lewejohann, L., Pan, Y., Fischer, T., Schlomann, U., Zhang, X., Esko, J.D., and Grobe, K. (2008). Altered heparan sulfate structure in mice with deleted *NDST3* gene function. *J. Biol. Chem.* 283, 16885–16894. <https://doi.org/10.1074/jbc.M709774200>.
- Randal, M., and Kossiakoff, A.A. (2001). The structure and activity of a monomeric interferon-gamma:alpha-chain receptor signaling complex. *Structure* 9, 155–163. [https://doi.org/10.1016/s0969-2126\(01\)00567-6](https://doi.org/10.1016/s0969-2126(01)00567-6).
- Salmela, L., and Schröder, J. (2011). Correcting errors in short reads by multiple alignments. *Bioinformatics* 27, 1455–1461. <https://doi.org/10.1093/bioinformatics/btr170>.
- Schmitz, S.K., Hjorth, J.J., Joemai, R.M., Wijntjes, R., Eijgenraam, S., de Bruijn, P., Georgiou, C., de Jong, A.P., van Ooyen, A., Verhage, M., et al. (2011). Automated analysis of neuronal morphology, synapse number and synaptic recruitment. *J. Neurosci. Methods* 195, 185–193. <https://doi.org/10.1016/j.jneumeth.2010.12.011>.
- Seifert, A.W., Kiama, S.G., Seifert, M.G., Goheen, J.R., Palmer, T.M., and Maden, M. (2012). Skin shedding and tissue regeneration in African spiny mice (*Acomys*). *Nature* 489, 561–565. <https://doi.org/10.1038/nature11499>.
- Simkin, J., Gawriluk, T.R., Gensel, J.C., and Seifert, A.W. (2017). Macrophages are necessary for epimorphic regeneration in African spiny mice. *Elife* 6, 26. <https://doi.org/10.7554/eLife.24623>.
- Steppan, S., Adkins, R., and Anderson, J. (2004). Phylogeny and divergence-date estimates of rapid radiations in muroid rodents based on multiple nuclear genes. *Syst. Biol.* 53, 533–553. <https://doi.org/10.1080/10635150490468701>.
- Streeter, K.A., Sunshine, M.D., Brant, J.O., Sandoval, A.G.W., Maden, M., and Fuller, D.D. (2020). Molecular and histologic outcomes following spinal cord injury in spiny mice, *Acomys cahirinus*. *J. Comp. Neurol.* 528, 1535–1547. <https://doi.org/10.1002/cne.24836>.
- Thuret, S., Thallmair, M., Horky, L.L., and Gage, F.H. (2012). Enhanced functional recovery in MRL/MpJ mice after spinal cord dorsal hemisection. *PLoS One* 7, e30904. <https://doi.org/10.1371/journal.pone.0030904>.
- Tica, J., and Didangelos, A. (2018). Comparative transcriptomics of rat and axolotl after spinal cord injury dissects differences and similarities in inflammatory and matrix remodeling gene expression patterns. *Front. Neurosci.* 12, 808. <https://doi.org/10.3389/fnins.2018.00808>.
- Tsata, V., Mollmert, S., Schweitzer, C., Kolb, J., Mockel, C., Bohm, B., Rosso, G., Lange, C., Lesche, M., Hammer, J., et al. (2021). A switch in *pdgfrb*+ cell-derived ECM composition prevents inhibitory scarring and promotes axon regeneration in the zebrafish spinal cord. *Dev. Cell* 56, 509–524.e9. <https://doi.org/10.1016/j.devcel.2020.12.009>.
- Wang, H., Katagiri, Y., McCann, T.E., Unsworth, E., Goldsmith, P., Yu, Z.X., Tan, F., Santiago, L., Mills, E.M., Wang, Y., et al. (2008). Chondroitin-4-sulfation negatively regulates axonal guidance and growth. *J. Cell Sci.* 121, 3083–3091. <https://doi.org/10.1242/jcs.032649>.
- Wu, C., Xue, Y., Wang, P., Lin, L., Liu, Q., Li, N., Xu, J., and Cao, X. (2014). IFN-gamma primes macrophage activation by increasing phosphatase and tensin homolog via downregulation of miR-3473b. *J. Immunol.* 193, 3036–3044. <https://doi.org/10.4049/jimmunol.1302379>.
- Yang, T., Dai, Y., Chen, G., and Cui, S. (2020). Dissecting the dual role of the glial scar and scar-forming astrocytes in spinal cord injury. *Front. Cell. Neurosci.* 14, 78. <https://doi.org/10.3389/fncel.2020.00078>.
- Zabbarova, I.V., Ikeda, Y., Carder, E.J., Wipf, P., Wolf-Johnston, A.S., Birder, L.A., Yoshimura, N., Getchell, S.E., Almansoori, K., Tyagi, P., et al. (2018). Targeting p75 neurotrophin receptors ameliorates spinal cord injury-induced detrusor sphincter dyssynergia in mice. *NeuroUrol. Urodyn.* 37, 2452–2461. <https://doi.org/10.1002/nau.23722>.

STAR★METHODS

KEY RESOURCES TABLE

REAGENT or RESOURCE	SOURCE	IDENTIFIER
Antibodies		
Rabbit polyclonal anti-5HT	ImmunoStar	Cat# 20080; RRID: AB_572263
Rabbit polyclonal anti-collagen type I	Rockland	Cat# 600-401-103-0.1; RRID: AB_2074625
Rabbit polyclonal anti-GFAP	Agilent	Cat# Z0334; RRID: AB_10013382
Rabbit polyclonal anti-MBP	Proteintech	Cat# 10458-1-AP; RRID: AB_2250289
Rabbit polyclonal anti-Ndst3	Thermo Fisher Scientific	Cat# PA5-63262; RRID: AB_2644540
Rabbit polyclonal anti-NGAL	Thermo Fisher Scientific	Cat# PA5-88079; RRID: AB_2804634
Rabbit polyclonal anti-SCG10	Novus Biologicals	Cat# NBP1-49461; RRID: AB_10011569
Rabbit polyclonal anti-Vglut1	Synaptic Systems	Cat# 135 303; RRID: AB_887875
Rabbit polyclonal anti-β3gnt7	Thermo Fisher Scientific	Cat# PA5-57342; RRID: AB_2638427
Rabbit polyclonal anti-βIII tubulin	Synaptic Systems	Cat# 302 302; RRID: AB_10637424
Mouse monoclonal anti-Heparan Sulfate (clone F58-10E4)	AMSBIO	Cat# 370255-1; RRID: AB_10891554
Mouse monoclonal anti-Keratan Sulfate (clone 5D4)	AMSBIO	Cat# 270427-1; RRID: AB_10920069
Mouse monoclonal anti-βIII tubulin	Promega	Cat# G7121; RRID: AB_430874
Alexa Fluor® 488-AffiniPure Goat Anti-Mouse IgG (H+L)	Jackson ImmunoResearch Labs	Cat# 115-545-003; RRID: AB_2338840
Alexa Fluor® 594-AffiniPure Donkey Anti-Mouse IgG (H+L)	Jackson ImmunoResearch Labs	Cat# 715-585-150; RRID: AB_2340854
Alexa Fluor® 488-AffiniPure Donkey Anti-Rabbit IgG (H+L)	Jackson ImmunoResearch Labs	Cat# 711-545-152; RRID: AB_2313584
Alexa Fluor® 594 AffiniPure Donkey Anti-Rabbit IgG (H+L)	Jackson ImmunoResearch Labs	Cat# 711-585-152; RRID: AB_2340621
Alexa Fluor® 568 Goat anti-Mouse IgM (Heavy chain) Cross-Adsorbed	Thermo Fisher Scientific	Cat# A-21043; RRID: AB_2535712
Bacterial and Virus Strains		
AAV1.CMV.PI.eGFP.WPRE.bGH	Penn Vector Core, University of Pennsylvania	N/A
pAAV-CMV>hB3GNT7[NM_145236.3] (ns):P2A:TurboGFP(ns):T2A:Puro:WPRE (VB210409-1218sw)	VectorBuilder	N/A
pAAV-CMV>EGFP:WPRE	VectorBuilder	N/A
Chemicals, Peptides, and Recombinant Proteins		
Ammonium chloride (NH ₄ Cl)	Merck	Cat# 1011450500
B27	Invitrogen	Cat #17504
Bovine serum albumin (BSA)	Sigma	Cat# A3294
Calcium chloride dehydrate (CaCl ₂ · 2H ₂ O)	Sigma	Cat# 10035-04-8
Collagenase-IV-S	Sigma	Cat# C1889
D-(+)-Glucose (C ₆ H ₁₂ O ₆)	Sigma	Cat# G8270
DMEM	Sigma	Cat# D6429-500ML
DMEM-F12	Sigma	Cat# D8437
Donkey serum	Sigma	Cat# D9663; RRID:AB_2810235
Fetal bovine serum (FBS)	Sigma	Cat# F9665
Formalin	Bio-optica	Cat# 05-K01004
Gelatin from cold water fish	Sigma	Cat# G7041

(Continued on next page)

Continued

REAGENT or RESOURCE	SOURCE	IDENTIFIER
Glycine	Merck	Cat# 1042011000
Heparinase III	AMSBIO	Cat# AMS.HEP-ENZ III-S
Ibidi Mounting Medium	Ibidi	Cat# 50001
Keratanase (Endo- β -Galactosidase)	Sigma	Cat# 345811
L-glutamine	Invitrogen	Cat# 25030024
Lipofectamine 2000	Thermo Fisher Scientific	Cat# 116678030
Magnesium chloride hexahydrate (MgCl ₂ * 6 H ₂ O)	Sigma	Cat# M2393
Neurobasal medium	Thermo Fisher Scientific	Cat# 21103-049
NGF	Millipore	Cat# 01-125
Paraformaldehyde (PFA)	Sigma	Cat# 158127
Penicillin/streptomycin	Thermo Fisher Scientific	Cat# 15140-122
Potassium chloride (KCl)	Sigma	Cat# 7447-40-7
PureBlu™ DAPI Nuclear Staining Dye	Bio-rad	Cat#1351303
Sodium bicarbonate (or Sodium hydrogen carbonate) (NaHCO ₃)	Sigma	Cat# 144-55-8
Sodium borohydride (NaBH ₄)	Sigma	Cat# 452882
Sodium chloride (NaCl)	Sigma	Cat# S9888
Sodium phosphate monobasic monohydrate (NaH ₂ PO ₄ · H ₂ O)	Sigma	Cat# 10049-21-5
Sucrose	Merck	Cat# 1076511000
Triton X-100	Sigma	Cat# T9284
Trypsin from porcine pancreas	Sigma	Cat# T4799

Critical Commercial Assays

NZY Total RNA Isolation kit	NZYtech	Cat# MB13402
NZY First-Strand cDNA Synthesis Kit,	NZYtech	Cat# MB125
Trichrome Stain (Masson) Kit	Sigma	Cat# HT15

Experimental Models: Organisms/Strains

<i>Acomys cahirinus</i>	N/A	N/A
<i>Mus musculus</i> : Adult C57BL/6	Charles River	N/A

Oligonucleotides

β 3gnt7; sense primer 5'- CCTCAAGGAGATCCACT -3'	This paper	N/A
β 3gnt7; anti-sense primer 5'- CCGTCAGACAGAACTC -3'	This paper	N/A
Ndst3; sense primer 5'- TGGTGTGGGTATCATTGG -3'	This paper	N/A
Ndst3; anti-sense primer 5'- TCCAGTCAGTTCCAGGTA -3'	This paper	N/A
Ndst4; sense primer 5'- GTCACCAGCACTGAAGAG -3'	This paper	N/A
Ndst4; anti-sense primer 5'- CTCCTGGATACTCCTTGT -3'	This paper	N/A
β 3galnt1; sense primer 5'- GCGTCAACTGGATGTAC -3'	This paper	N/A
β 3galnt1; anti-sense primer 5'- CTCTAATGGCTTGTCTGG -3'	This paper	N/A
Sdha; sense primer 5'- TGTTCAAGTCCACCCAC -3'	This paper	N/A
Sdha; anti-sense primer 5'- TCTCCACGACATCCTTCTGT -3'	This paper	N/A

(Continued on next page)

Continued

REAGENT or RESOURCE	SOURCE	IDENTIFIER
Software and Algorithms		
Axiovision imaging software	Zeiss	RRID:SCR_002677
Beacon designer software	Biosoft	N/A
Fiji	NIH	RRID:SCR_002285
GraphPad Prism 6	GraphPad	RRID:SCR_002798
Leica LAS X software	Leica	RRID:SCR_013673
Olympus Cell software	Olympus	RRID:SCR_014342
Synapse Detector (SynD)	(Schmitz et al., 2011)	N/A
Others		
Axio Imager microscope	Zeiss	RRID:SCR_018856
CFX384 Touch™ Real-Time PCR Detection System	Bio-rad	N/A
Cryostat Leica CM 3050 S	Leica	RRID:SCR_020214
IN Cell Analyzer 2000 microscope	GE Healthcare	N/A
Isolated pulse stimulator	A-MSystems	RRID:SCR_016677
Leica DMI6000 B	Leica	RRID:SCR_018713
Motorized stereotaxic microinjector	Stoelting	N/A
Olympus light microscope	Olympus	RRID:SCR_017564

RESOURCE AVAILABILITY

Lead contact

Further information and requests for resources and reagents should be directed to and will be fulfilled by the lead contact, Monica M Sousa (msousa@ibmc.up.pt).

Materials availability

This study did not generate new unique reagents.

Data and code availability

All data generated and analyzed during this study are included in this published article (and its [supplemental information](#) files) and available from the corresponding author upon reasonable request. The raw data on *Acomys* transcriptome reconstruction is deposited in SRA (BioProject: PRJNA766650, accessions SRR16088842 to SRR16088857).

EXPERIMENTAL MODELS AND SUBJECT DETAILS

Animals

All animals were handled and euthanized according to the European Union Directive 2010/63/EU and the national Decreto-lei n° 113-2013. The protocols here described have been approved by the i3S Ethical Committee and by the Portuguese Veterinarian Board. *Mus musculus* (C57BL/6) were bred and provided by the animal house facility of the i3S. *Acomys cahirinus* were bred at the animal house facility of the University of Algarve, Portugal. All animals were maintained with *ad libitum* access to water/food, and kept on a 12 hour light/dark cycle. Only adult (12-16 weeks old) females were used for SCI experiments.

Cell lines

Confluent monolayers of Chinese Hamster Ovary cells (CHO) were maintained in 75 cm² cell culture flasks at 37 °C in DMEM medium (Sigma, D6429-500ML), supplemented with 10 % FBS (Sigma, F9665) and 1% penicillin/streptomycin (Thermo Fisher Scientific, 15140-122). CHO cells were split into 4-well chambers slides (IBIDI, 80426) and following 3-4 days in culture, they were transfected with a plasmid leading to the overexpression of hβ3GNT7 linked to TurboGFP (pAAV-CMV>hB3GNT7[NM_145236.3]:P2A:TurboGFP:T2A:Puro:WPPE; VectorBuilder) or a similar empty vector leading to the overexpression of TurboGFP (pAAV-CMV>EGFP:WPPE; VectorBuilder) using Lipofectamine 2000 (Thermo Fisher Scientific, cat# 116678030) and grown for 3-4 days.

Primary cultures

DRG neuron cultures were performed as detailed in [Leite et al. \(2016\)](#). Briefly, DRG were collected from 3-4 weeks old *Mus* and digested with 0.125% collagenase-IV-S (Sigma, C1889) for 90 minutes at 37°C with 5% CO₂, dissociated into a single cell suspension

by gentle trituration and centrifuged in a 15% BSA (Sigma, A3294) gradient. DRG neurons were plated at 5000 cells/well on top of CHO cells previously established in 4-well chambers slides (IBIDI, 80426). Culture medium was DMEM:F12 (Sigma, D8437) supplemented with 1x B27 (Invitrogen, 17504), 1% penicillin/streptomycin (Thermo Fisher Scientific, 15140-122), 2 mM L-glutamine (Thermo Fisher Scientific, 25030024) and 50 ng/mL NGF (Millipore, 01-125). The co-culture was maintained at 37°C with 5% CO₂ for 24h.

Similar experiments were performed using embryonic cortical neurons cultures. Cortical tissues were obtained from the brains of E18 mouse embryos and cultured as described in Dent et al. (1999) and Mar et al. (2016). Briefly, cortical tissue was digested 15 min at 37°C in 0.06% trypsin (Sigma-Aldrich, T4799) and then centrifuged. *Mus* cortical neurons (25 000 cells/well) were plated onto CHO cells previously established in 4-well chambers slides (IBIDI, 80426). Cortical neurons were cultured in Neurobasal medium (Thermo Fisher Scientific, 21103-049) supplemented with 1x B27 (Invitrogen, 17504), 1% penicillin/streptomycin (Thermo Fisher Scientific, 15140-122) and 2 mM L-glutamine (Thermo Fisher Scientific, 25030024). The co-culture was maintained at 37°C with 5% CO₂ for 24h.

METHOD DETAILS

Spinal cord injury and post-surgical animal care

Adult (12-16 weeks old) female *Mus* and *Acomys* were deeply anesthetized with continuous inhalation of isoflurane (Isovet, B Braun, 469860). Laminectomy was performed at the thoracic vertebrae T7-79 and a complete transection of the spinal cord was done at T8 using a micro feather ophthalmic scalpel (Feather, Safety Razor Co. Ltd). Sham female animals of both genera were used to serve as controls. Analgesia was performed for 72 hours with buprenorphine twice a day (3 mg/kg). At 8WPI, injured *Acomys* (n=4) were re-injured (complete spinal cord transection) at T8 as previously performed. Upon surgery, animals were supplemented with fresh fruit twice a week and fed with Anima-Strath®. Only female animals were used for SCI experiments as females have less urinary infections and bladder management is easier. Bladder management was done by gentle abdominal compression, twice-daily until voluntary micturition was observed. Unless stated otherwise, all animals were euthanized at 8WPI; AAV-injected animals were euthanized at 12 WPI and re-injured *Acomys* at 16WPI.

Functional evaluation

All functional analyses were performed at 2, 4 and 7 days and weekly for 8 WPI (or 16 WPI in the case of re-injured *Acomys*). Hindlimb locomotor function was assessed using the Basso Mouse Scale (BMS) (Basso et al., 2006). Briefly, patterns of hind limbs movement, plantar stepping and paw positions were observed in a 5 min session per animal. All *Mus* (n=14) and *Acomys* (n=14) were habituated to the BMS open-field arena in 10 min sessions every day for 1 week. The locomotor score was given by two blinded independent observers. To evaluate bladder function, the urine spot test was performed. Each animal was placed in a clean metabolic cage lined with blotting filter paper at the bottom (Whatman, 3030-917) for 30 min without access to water or food during the assay as described (Chen et al., 2017; Zabbarova et al., 2018). The filter papers were visualized under UV light of a Gel-Doc-XR (Bio-Rad), images were saved as TIFF files and the urine spot areas were analyzed using Fiji software. To make a calibration curve, the areas of different volumes of water were also measured with Fiji. For all the animals where functional analysis is provided, following the final timepoint of recovery, the completeness of spinal cord transection was confirmed by the observation of all longitudinal sagittal sections comprising the entire spinal cord. Only animals where complete injury was observed in all the sections have been included in the study.

Histology and immunofluorescence analysis

In all animals, axon regeneration was analyzed at 8 WPI or at 12 WPI (for AAV-injected animals). The same reagents and antibodies were used for both *Mus* and *Acomys* spinal cords. *Mus* and *Acomys* were transcardially perfused with 10% formalin (Bio-optica, 05-K01004) and the spinal cords were post-fixed for 1 week at 4°C and later cryoprotected in 30% sucrose and processed using a Cryostat Leica CM 3050 S (RRID:SCR_020214) (section thickness of 50 μm for free floating immunohistochemistry and 10 μm for slide-mounted frozen cryosections). Serial sagittal spinal cord sections containing the lesion site and rostral and caudal cross sections were collected for each animal. Only animals where a complete injury was confirmed by observation of all longitudinal sagittal sections were analyzed. Sagittal cryosections (50 μm) were incubated with 0.1M glycine (Merck, 1042011000) overnight at 4°C, permeabilized with 1% Triton X-100 (Sigma, T9284) for 20 min, incubated with 0.2M NH₄Cl (Merck, 1011450500) for 20 min and then incubated with 0.1% NaBH₄ (Sigma, 452882) for 5 min. Sections were blocked with 1 mg of BSA (Sigma, A3294) and 1% Triton X-100 for 1 h at room temperature (RT) and then incubated for 48 h at 4°C with the following primary antibodies: mouse anti-βIII tubulin (Promega, G7121; 1:1000; RRID:AB_430874), rabbit anti-SCG10/Stathmin-2 (Novus Biologicals, NBP1-49461; 1:5000; RRID:AB_10011569; a marker of regenerating sensory axons (Mori et al., 2006)), rabbit anti-collagen type I (Rockland, 600-401-103-0.1; 1:750; RRID:AB_2074625), rabbit anti-gliar fibrillary acidic protein (Agilent, Z0334; 1:2000; RRID:AB_10013382) and rabbit anti-myelin basic protein (Proteintech, 10458-1-AP; 1:1500; RRID:AB_2250289). Secondary antibodies included: Alexa Fluor 488 AffiniPure goat anti-mouse (Jackson ImmunoResearch Laboratories, 115-545-003; 1:1000; RRID:AB_2338840) and Alexa Fluor 594 AffiniPure donkey anti-rabbit (Jackson ImmunoResearch Laboratories, 711-585-152; 1:1000; RRID:AB_2340621). Serotonergic axons were visualized in cross/sagittal sections (50 μm) incubated with 0.2M NH₄Cl for 30 min and blocked with 10% donkey serum (Sigma, D9663) and 0.3% Triton X-100 for 1 h at RT, and incubated with rabbit anti-5-hydroxytryptamine (5-HT) primary antibody (ImmunoStar, 20080; 1:5000; RRID:AB_572263) for 48 h at 4°C.

Sections were then incubated for 2 h with Alexa Fluor 594 AffiniPure donkey anti-rabbit (Jackson ImmunoResearch Laboratories, 711-585-152; 1:1000; RRID:AB_2340621). To identify synaptic boutons in close proximity to CST axons (previously labelled with AAV injection as detailed below), sagittal sections (50 μm) were blocked with a mixture of 2% fish gelatin (Sigma, G7041), 2% BSA and 2% fetal bovine serum (FBS) (Sigma, F9665) for 1 h at RT and incubated with rabbit anti-vGlut1 primary antibody (Synaptic System, 135 303; 1:500; RRID:AB_887875) overnight at 4°C. Sections were then incubated for 2 h with Alexa Fluor 594 AffiniPure donkey anti-rabbit (Jackson ImmunoResearch Laboratories, 711-585-152; 1:500; RRID:AB_2340621). For the analysis of ECM proteoglycans, glycosylation-related enzymes and astrocytes immunofluorescence was performed in sagittal slide-mounted frozen cryosections (10 μm) that were permeabilized with ice-cold methanol for 15 min, incubated with 0.5% Triton X-100 for 20 min and with 0.2 M NH_4Cl for 20 min. Sections were blocked with 2% BSA for 1 h at RT and incubated overnight at 4°C with the following primary antibodies: mouse anti-keratan sulfate (clone 5D4) (Amsbio, 270427-CS; 1:50; RRID:AB_10920069), mouse monoclonal anti-heparan sulfate (clone F58-10E4) (Amsbio, 370255-1; 1:150; RRID:AB_10891554), rabbit polyclonal anti- β3gnt7 (Thermo Fisher Scientific, PA5-57342, 1:100; RRID:AB_2638427), rabbit polyclonal anti-Ndst3 (Thermo Fisher Scientific, PA5-63262, 1:200; RRID:AB_2644540) and rabbit polyclonal anti-NGAL (LCN2) (Thermo Fisher Scientific, PA5-88079, 1:200; RRID:AB_2804634). Sections were incubated for 1 h at 4°C with the secondary antibodies: Alexa Fluor 568 AffiniPure goat anti-mouse IgM, μ chain specific (Thermo Fisher Scientific, A-21043; 1:100; RRID:AB_2535712) and Alexa Fluor 594 AffiniPure donkey anti-mouse IgG (Jackson ImmunoResearch Laboratories, 715-585-150; 1:100; RRID:AB_2340854). For enzymatic digestions, prior to immunofluorescence, sections were incubated with heparinase III (EC 4.2.2.8; 5 mU/ml; Amsbio, AMS.HEP-ENZ III-S) or keratanase (endo- β -galactosidase; ≥ 14 U/ml; Sigma, 345811) for 2h at 37°C. To visualise connective tissue composition, sagittal sections (10 μm) were stained with Masson trichrome staining (Sigma, HT15). All histological analyses were randomized and performed blinded to the genus of the animal. All spinal cord sections were used under the same exposure for the same antibodies. Image acquisition was performed using the IN Cell Analyzer 2000 microscope (GE Healthcare) at 20x magnification with acquisition software v4.5. and with an Axio Imager microscope (Zeiss, RRID:SCR_018856) at 20x and 40x magnification with an Axiocam MR3.0 camera and Axiovision imaging 4.7 software (Zeiss, RRID:SCR_002677), and subsequently analyzed in Fiji software (RRID:SCR_002285). Analysis of β III-tubulin-positive axonal regeneration was performed by assessing the number of axons penetrating or growing inside the lesion core in 20x magnification images of spinal cords from *Mus* (n=7) and *Acomys* (n=7), in 7-17 sections per animal. Regeneration of 5-HT fibers in spinal cord cross sections was assessed by measuring the mean pixel value of fluorescence intensity (the background was subtracted) inside a marked area spanning around the ventral part of the grey matter of rostral and caudal sections of *Mus* (n=6) and *Acomys* (n=6) spinal cords. In spinal cord sagittal sections, the total number and axon regeneration distance of 5-HT-positive axons growing within the injury site was assessed by using a vertical line placed at the rostral end of the lesion border perpendicularly to the sagittal axis of each spinal cord of *Mus* (n=3) and *Acomys* (n=6), in at least 8 sections per animal. Glycosylation related-enzymes and ECM proteoglycan fluorescence intensity was measured from uninjured and injured *Mus* and *Acomys* (n=4-6 each genus) spinal cord images at 20x magnification (2-6 sections of each spinal cord/animal). For β3gnt7 and Ndst3 the mean pixel value of fluorescence intensity in the lesion site was measured. For the quantification of KSPG deposition in uninjured and injured *Mus* and *Acomys* (n=4-6 each genus), the total area containing KSPG-positive staining (similar to a honeycomb-like structure) was measured in each section (2-4 sections of each spinal cord/animal); for KSPG, normalization in relation to distal caudal and rostral stumps was not performed as staining was negligible in all groups except in *Acomys* following SCI. For HSPG, the mean pixel value of fluorescence intensity was measured in the region of the lesion site and the ratio relative to the staining in proximal and distal spinal cord stumps was calculated. GFAP and col I fluorescence intensity were assessed from injured *Mus* and *Acomys* (n=7, each genus for GFAP and n=6 for col I) at 20x magnification by measuring the mean pixel value of fluorescence intensity of the same ROI in each section (2-4 sections of each spinal cord/animal). Analysis of gray/white matter ratios in cross sections of sham animals was performed by measuring pixel area of total, gray and white matter area in spinal cord cross sections (3-6 sections) in *Mus* (n=2) and *Acomys* (n=2). Images were acquired using a light microscope Olympus (RRID:SCR_017564) with an Olympus DP 25 camera and Cell B software (RRID:SCR_014342).

AAV injection for anterograde tracing

For tracing of the descending CST, injured *Mus* (n=3) and *Acomys* (n=2) were injected intracortically with an AAV1/2 vector leading to the expression of eGFP under the CMV promoter (AAV1.CMV.PI.eGFP.WPRE.bGH, 5.738×10^{13} GC/ml, Penn University - in the text referred as AAV1/2-eGFP) at 8 WPI. This timepoint of viral injection was chosen as viral injections at 4WPI could influence functional analysis. Animals were deeply anesthetized with isoflurane and positioned in a stereotaxic device with motorized stereotaxic microinjector (Stoelting). Following a midline incision, the bregma was exposed and four holes were drilled in the right sensorimotor cortex. For *Mus*, the coordinates were as described (Du et al., 2015; Jin et al., 2015); in *Acomys* the following coordinates were used: anteroposterior/mediolateral: 1.35/-1.0 and 1.35/-2.6 (1.4mm DV); 0.63/-0.7 and 0.63/-2.2 (1.2mm DV). The injections were performed using a 10 μl Hamilton syringe (Series 1700 Hamilton). Once the needle was at the appropriate depth, 0.3 μl of virus were injected in each coordinate (0.1 μl /min). After the injection, the syringe was left for 2 minutes to avoid leakage. Four weeks later, the animals were euthanized i.e., at 12 WPI.

Electrophysiology

Uninjured *Mus* (n=5) and *Acomys* (n=4), and injured *Mus* (n=3) and *Acomys* (n=10) were terminally anaesthetized with an i.p. injection of 50 mg/kg of pentobarbital at 8 WPI. Spinal cord from the upper cervical to lower lumbar levels was quickly removed, cleaned from the meninges and nerve roots, and kept in artificial cerebrospinal fluid (aCSF) containing: 115 mM NaCl (Sigma, S9888), 3 mM KCl

(Sigma, 7447-40-7), 2.2 mM CaCl₂ (Sigma, 10035-04-8), 1 mM MgCl₂ (Sigma, M2393), 1 mM NaH₂PO₄ (Sigma, 10049-21-5), 25 mM NaHCO₃ (Sigma, 144-55-8) and 11 mM glucose (Sigma, G8270) (bubbled with 95% O₂ and 5% CO₂). The spinal cord was transferred to the recording chamber perfused with oxygenated aCSF and allowed to recover for at least 45 min. All recordings were done at a temperature of 22–24°C. Suction electrodes fabricated from thick-walled glass (BioMedical Instruments, Germany) were used for both stimulation and recording. To study CAP conduction in descending motor tracts, the lateral funiculus of each side of the spinal cords (right/left) was stimulated at a location 8–10 mm rostral to the lesion site (Stim. A; Figure 2L) using the Isolated Pulse Stimulator (2100, A–M Systems, RRID:SCR_016677). Two recording electrodes were positioned 4–5 mm rostrally (Rec. B; Figure 2L) and 4–5 mm caudally to the lesion (Rec. C; Figure 2L), to compare CAP amplitudes before and after crossing the lesion site, thus revealing functional fibers crossing the scar. The recording electrode Rec.B allowed to control the viability of the spinal cord preparation and the proper propagation of CAPs. Each suction electrode had its own reference electrode. Spinal cords were stimulated with a 50 μs pulse of 200 μA at a 3s interval. For recording, we used the differential AC amplifier (1700, A–M Systems), in which the low cut-off filter was set 0.1 Hz. The signal was online low-pass filtered at 10 kHz and sampled using the A/D converter of the EPC9 amplifier (HEKA, Lambrrecht, Germany). Of note, only injured *Acomys* that recovered weight support and presented locomotor recovery (BMS > 5) were used. Quantification of CAP conduction was performed by measuring the amplitude for each animal with the average of at least 10 traces.

RNA extraction and transcriptomic analysis

At 8 WPI, the lesion site (4–5 mm) from 4 injured *Mus* and 4 injured *Acomys* was collected and total RNA was extracted using NZY total RNA isolation kit (MB13402). Thoracic spinal cord sites from sham animals (n=4 *Mus* and n=4 *Acomys*) were also collected to serve as controls. RNA concentration and purity was determined by NanoDrop® spectrophotometry, and integrity was confirmed using Expiration RNA StdSens Kit (Bio-Rad). Preparation of barcoded stranded RNAseq libraries and deep uni-directional sequencing (read-length: 75 bases; yield: ~550 million of paired sequence reads; FASTQ files have been deposited under BioProject: PRJNA766650, accessions SRR16088842 to SRR16088857) were performed at the Genomics Core Facility (GeneCore) at EMBL, Heidelberg, Germany. Since these two species have been diverging for 20 million years (Steppan et al., 2004), and non-coding regions evolve faster than coding regions, the expression of coding sequence (CDS) isoforms (rather than transcript isoforms) was compared. Although the *Acomys cahirinus* genome has been sequenced (https://www.ncbi.nlm.nih.gov/assembly/GCA_004027535.1/), there is no genome annotation available, and thus, *Acomys* transcriptome was assembled using all available data at the NCBI SRA database (<https://www.ncbi.nlm.nih.gov/sra>) and data collected in this work. The average read quality of all datasets was evaluated using Fastqc. Docker images and all other software applications here used are available at the pegi3s Bioinformatics Docker Images Project (<https://pegi3s.github.io/dockerfiles/>). The SRA datasets that were considered suitable for the transcriptome reconstruction are: SRR636836, SRR636837, SRR636838, SRR2146799, SRR2146800, SRR2146801, SRR2146802, SRR2146803, SRR2146804, SRR2146805, SRR2146806, SRR2146807, SRR2146808, SRR2146809, SRR2146810, SRR2146811, SRR2146812, SRR2146813, SRR2146814, SRR2146815, SRR2146816, SRR2146817, SRR2146818, SRR2146819, SRR2146820, SRR2146821, SRR2146822, SRR2146823, SRR2146824, SRR2146825, SRR2146826, SRR2146827, SRR2146828, SRR2146829, SRR2146830, SRR2146831, SRR2146832, SRR2146833, SRR2146834, SRR2146835, SRR2146836, SRR2146837, SRR2146838, SRR2146839, SRR2146840, SRR2146841, SRR2146842, SRR2146843, SRR3623231, SRR3623232, SRR3623233, SRR3623234, SRR3623235, SRR3623236, SRR3623237, SRR3623238, SRR3623239, SRR3623240, SRR4279903, SRR4279904, SRR6994950, SRR6994951, SRR6994952, SRR6994953, SRR6994954, SRR6994955, SRR6994956, SRR6994957, SRR6994958, SRR6994959, SRR6994960, SRR6994961, and SRR6994962. Cutadapt (Martin, 2011) was used to trimmed the first 20 positions of each read (usually of lower quality). FASTQ files were transformed into FASTA files (using Docker image), and all Forward (F) and Reverse (R) read files concatenated separately. At this point, both F and R FASTA files contain 1,326,395,625 reads. Reads showing ambiguous positions, as well as their respective mates, were removed (51,012,743 and 2,929,801 reads from the F and R files, respectively). After this filtering step, there were 1,273,100,625 reads on both F and R FASTA files. The average read quality for each of the 8 *Acomys* FASTQ files was assessed using Fastqc and the first 15 positions of each read trimmed using cutadapt. The resulting FASTQ files were transformed into FASTA files (using Docker image) and the files concatenated. Reads showing ambiguous positions were removed. After this, there were 241,370,110 read sequences in the FASTA file. Coral (Salmela and Schroder, 2011) was used to correct reads at positions showing variability in read alignments. This file was then used to correct, using Coral, the F and R FASTA files mentioned above, as well as the 8 *Acomys* FASTQ files here obtained. All corrected files were used to perform a transcriptome assembly using Trinity (Haas et al., 2013) (468,445,830 reads were kept out of 1,273,100,625, i.e. 36.80%). The reconstructed *Acomys cahirinus* transcriptome is represented by 1,053,074 sequences, but it is unlikely that every sequence represents a full-length transcript. The EMBOSS getorf software application was used to extract the longest ORF from the reconstructed sequences. For *Mus*, the average read quality for each of the 8 FASTQ files here obtained was evaluated using the Fastqc software application. As for *Acomys*, the first 15 positions of each read were trimmed using cutadapt, and the resulting FASTQ files were transformed into FASTA files and concatenated. Reads showing ambiguous positions were then removed, resulting in a 296,236,846 read sequences file. Coral was then used to correct reads at positions showing variability in read alignments. The resulting file was then used to correct, using Coral, the file containing all annotated *Mus* CDS in the reference genome (GCF_000001635.27) that was downloaded from the NCBI RefSeq database (<https://www.ncbi.nlm.nih.gov/assembly>), as well as the 8 *Mus* FASTQ files here obtained were corrected. SEDA (Lopez-Fernandez et al., 2020) was used to retain only *Acomys* CDS isoforms having an orthologue *Mus* sequence (identified using the “BLAST two-way ortholog” operation), that show less than 20% size difference relative to the *Mus* orthologous CDS, with a start codon and no in-frame

stop codons. 15,827 CDS isoforms were compared between *Mus* and *Acomys*. FPKM values were estimated using the RSEM method, as implemented in Trinity, the reconstructed *Acomys* transcriptome and the paired *Mus* transcriptome, and the corrected and filtered read files here obtained for sham/injured *Mus/Acomys*. Differentially expressed CDS isoforms were identified using voom (Law et al., 2014) and the four available biological replicates for each condition. CDS isoforms that have P-values at most 10^{-3} and are at least $2^{2.2}$ fold were extracted and heatmaps produced. The differentially expressed CDS isoforms were partitioned into clusters with similar expression patterns by cutting the hierarchically clustered gene tree at 10% the height of the tree. Only Trinity clusters for which more than 75% of the members show a statistically significant difference between conditions were selected. PANTHER was used to identify overrepresented gene categories.

To validate transcriptomics of SCI sites, 200 ng of total RNA sample were used to synthesize first-strand cDNA (NZY First-Strand cDNA Synthesis Kit, MB125). SYBR-green quantitative PCR (CFX384 Touch™ Real-Time PCR Detection System, Bio-rad) was performed using species-specific primers (the sequence of species-specific PCR primers is detailed in the key resources table). Primers were designed to bind orthologous regions of each gene in both species (similar GC content and PCR product size) using the Beacon designer software (Biosoft). The fold change in gene expression was calculated using the $\Delta\Delta\text{Ct}$ relative expression method (Livak method) and primers for *Sdha* were used as the endogenous control and calculated separately for each sample and respective species/condition.

Neurite outgrowth assay

Neurite outgrowth was assessed following immunofluorescence against β III-tubulin. DRG and cortical neuron cultures of *Mus* were plated on top of transfected CHO and fixed at DIV1 with 2% paraformaldehyde (PFA) (Sigma, 158127) for 10 min at RT, followed by cell membrane permeabilization (0.1% Triton X-100) and blocking with 5% FBS in phosphate-buffered saline (PBS) for 1 hour at RT. Incubation with rabbit anti- β III-tubulin (Synaptic Systems 302 302; 1:1000, RRID:AB_10637424) was done overnight at 4°C. The secondary antibody donkey anti-rabbit Alexa Fluor 594 (Jackson ImmunoResearch, 711-585-152; 1:1000, RRID:AB_2340621) was used for 1 hour at RT. Four-well cell chambers were incubated with DAPI for 15min (Bio-rad, #1351303). Images were acquired in a Leica DMI6000 B (Leica, RRID:SCR_018713) equipped with an Hamamatsu FLASH4.0 digital camera and Leica Application Suite Advanced Fluorescence (LAS AF) software (RRID:SCR_013673). Total neurite length was assessed in Matlab (RRID:SCR_001622) with Synapse Detector (SynD) software (Schmitz et al., 2011) and Fiji software. Only DRG or cortical neurons grown on top of transfected CHO cells were considered for analysis. A total of 3 independent experiments were analyzed for each cell type.

QUANTIFICATION AND STATISTICAL ANALYSIS

Data is shown as mean and standard error of the mean (SEM). The statistical analysis for all experiments was performed with GraphPad Prism 6 (RRID:SCR_002798). Unless elsewhere stated, the following statistical tests were used as indicated in figure legends: two-tailed unpaired or paired t-test, one-way or two-way ANOVA followed by Tukey's multiple comparison test for samples with Gaussian distribution. Two-tailed Mann-Whitney t-test and Kruskal-Wallis test followed by Dunn's multiple comparison test were used for samples without Gaussian distribution. Sample sizes are indicated in figure legends and significance was defined as p value* <0.05 , ** <0.01 , *** <0.001 , **** <0.0001 , ns: not significant.